Stability of the Dual-Frequency Radar Equations and a New Method Applied to the GPM's Dual-Frequency Precipitation Radar (DPR) Data

Toshio Iguchi, *Fellow, IEEE*, and Robert Meneghini, *Senior Member, IEEE*

***Abstract*— A new algorithm is proposed, which estimates two parameters of the particle size distribution (PSD) at each range bin from the global precipitation measurement's (GPM's) dual-frequency precipitation radar (DPR) data. The equation that expresses the relationship of the PSD parameters between adjacent range bins is derived. By including the attenuation effect within the bin in the discretized equation, the new algorithm alleviates the double-solution problem when attenuation within the bin is sufficiently large. The stability of the solutions to the equation depends on the value of the mean diameter D_m and its gradient with respect to the range in the case of liquid precipitation. There is a critical diameter above which the backward processing of the equation provides a stable or moderately diverging solution, unlike the forward processing that often gives unstable solutions. To provide a set of initial conditions without using the surface reference technique (SRT) in the backward processing, an initialization method using the Hitschfeld–Bordan (HB) attenuation correction method is proposed and tested. The proposed algorithm may provide a tool for investigating the assumptions used in various algorithms.**

***Index Terms*— Dual-frequency precipitation radar (DPR), global precipitation measurement (GPM), particle size distribution (PSD), rainfall rate.**

I. Introduction

THE dual-frequency precipitation radar (DPR) onboard the core satellite of the global precipitation measurement (GPM) mission consists of a Ku-band radar (KuPR) and a Ka-band radar (KuPR) [1]. It was designed to measure backscatter by precipitation in the same scattering volumes at two different frequencies so that it would be able to provide two independent pieces of information about the scattering characteristics of the particles at each scattering volume. The effective radar reflectivities at the Ku- and Ka-bands differ slightly due to the fact that the non-Rayleigh scattering effect, or size effect, is more pronounced at the Ka-band than at the Ku-band. More specifically, if we denote the radar reflectivity factor in dB units at the Ku-band by $\mathrm{dB}Z_{e1}$ and that at the Ka-band by $\mathrm{dB}Z_{e2}$, this difference appears in the dual-frequency ratio (DFR) that is defined as

$$\mathrm{DFR} \stackrel{\mathrm{def}}{=} \mathrm{dB}Z_{e1} - \mathrm{dB}Z_{e2}. \tag{1}$$

Hereafter, subscripts 1 and 2 are used to indicate Ku- and Ka-band parameters, respectively. (Nevertheless, $\mathrm{dB}Z_e$ for Ku- and Ka-bands are also written as $\mathrm{dB}Z_e$(Ku) and $\mathrm{dB}Z_e$(Ka), respectively, in later sections to increase readability.) If we characterize the distribution of precipitation particle size by two parameters, one with the mean diameter D_m and the other with a quantity N_0 that is proportional to the number density N_t, all radar parameters can be expressed as functions of D_m and N_0 provided that other physical and scattering properties of particles are known. Under such conditions, since Z_{e1} and Z_{e2} are linearly proportional to N_0, DFR becomes a function of D_m alone. Therefore, once DFR is obtained, D_m is expected to be estimated by using the inverse function of $\mathrm{DFR}(D_m)$.

This logic is the basic idea of estimating D_m by a matched-beam dual-frequency radar. Its feasibility for snow parameter estimation was shown by airborne radar data [2]. Nevertheless, after the launch of the GPM satellite, it turned out that estimating D_m independently at each range bin was a formidable task. The reasons for the difficulty are multifold. The major difficulty lies in the accurate attenuation correction without the accumulation of biases at either frequency. In order to calculate DFR, we need to estimate Z_{e1} and Z_{e2} from measured radar reflectivity factors Z_{m1} and Z_{m2} by correcting the attenuations. To correct for the attenuation, we need to know the specific attenuations k_1 and k_2 at each range, but, to know them, we need D_m and N_0. Although it is theoretically possible to estimate the attenuation from the nearest range bin to the next successively by solving the equations that relate $Z_m(r)$, $Z_e(r)$, and $k(r)$ to $D_m(r)$ and $N_0(r)$, this self-referencing nature of equations tends to accumulate errors in one direction and often gives unreasonable estimates of D_m and N_0. There are several error sources that cannot be totally eliminated. They include noise and fluctuation in measured signals, calibration errors, differences between the assumed particle size distribution (PSD) models and the actual PSD, and other assumptions, such as environmental conditions [3].

Attenuation correction by using the path-integrated attenuation (PIA) estimated by the surface reference technique (SRT) [4] is possible and enables an estimation of the DFR at each range bin starting from the last gate of the column and

Manuscript received August 19, 2021; revised November 19, 2021 and January 28, 2022; accepted March 11, 2022. Date of publication March 14, 2022; date of current version April 12, 2022. This work was supported by the National Aeronautics and Space Administration (NASA) under Grant NNX17AI84A. *(Corresponding author: Toshio Iguchi.)*

Toshio Iguchi is with ESSIC, University of Maryland, College Park, MD 20740 USA (e-mail: tiguchi@umd.edu).

Robert Meneghini is with the NASA Goddard Space Flight Center, Greenbelt, MD 20771 USA.

Digital Object Identifier 10.1109/TGRS.2022.3159396

progressing backward. However, because of other concerns and the difficulty of estimating D_m reliably in many cases, the initial operational algorithms (V04, V05, and V06) use a conservative approach in which D_m is not estimated independently at each range [5]. The operational algorithms are those used to produce the operational GPM products disseminated by National Aeronautics and Space Administration (NASA) and Japan Aerospace Exploration Agency (JAXA). They are called standard algorithms, and their products are called standard products in this article.

This article examines the general properties of PSD parameter estimation and proposes a new algorithm that estimates D_m and N_0 at each range. Section II reviews a differential form of the PSD estimation equation and its properties. Section III introduces discretized equations that include the effect of attenuation within the range bin in which the PSD parameters are estimated. By including the attenuation effect within the bin, the double-solution problem is partly mitigated. Section IV describes the general characteristics of the algorithm that includes how the dual-solution problem is mitigated. Section V shows a few examples of PSD parameters estimated from DPR data with this algorithm. Section VI discusses the issues of the PSD estimation. Section VII summarizes this article.

II. Differential Equations for Two PSD Parameters

A. Formulation of the Problem

We assume that rain is uniform in the lateral directions perpendicular to the range direction of radar so that the measurement of rain echo can be treated as a 1-D problem. Under this assumption, the expected value of the measured radar reflectivity factor Z_m, in dB units (dBZ_m), at range r can be expressed in terms of the effective radar reflectivity factor Z_e, in dB units (dBZ_e), and an attenuation factor given as the integral of the specific attenuation k

$$\mathrm{dB}Z_{m\lambda}(r) = \mathrm{dB}Z_{e\lambda}(r) - 2\int_{r_0}^{r} k_\lambda(s)\,ds, \quad (\lambda = 1, 2) \tag{2}$$

where k is expressed in dB per unit length and r_0 is the range at which the radar echo starts. Since we assume that we measure the same rain profiles at two frequencies, any parameters at these frequencies are distinguished by subscript λ, where $\lambda = 1, 2$. Both Z_e and k are functions of the PSD $N(D)$. If $N(D)$ can be well approximated by a model function $N_m(D)$ with two parameters θ_1 and θ_2, both Z_e and k become functions of these two parameters. They can be expressed mathematically as follows:

$$Z_{e\lambda}(\theta_1, \theta_2) = c_{Z\lambda}\int \sigma_{b\lambda}(D) N_m(D; \theta_1, \theta_2)\,dD \tag{3}$$

and

$$k_\lambda(\theta_1, \theta_2) = c_k \int \sigma_{t\lambda}(D) N_m(D; \theta_1, \theta_2)\,dD. \tag{4}$$

Here, $\sigma_{b\lambda}$ is the backscattering cross section, and $\sigma_{t\lambda}$ is the extinction cross section. The coefficient $c_{Z\lambda}$ is defined by $c_{Z\lambda} = \lambda^4/(\pi^5|K_\lambda|^2)$ with $K_\lambda = (m_\lambda^2 - 1)/(m_\lambda^2 + 2)$ where m_λ is the complex refractive index of the particle for electromagnetic waves with wavelength λ. c_k is a proportional constant that changes with the unit of k_λ. Since we use the unit of k_λ as dB per unit length, as in (2), $c_k = 1/q$, where $q = 0.1\ln(10)$ is the conversion factor from dB to neper.

Taking the logarithm of (2) and differentiating it with respect to r, we obtain

$$\frac{d\mathrm{dB}Z_{m\lambda}}{dr} = -2k_\lambda + \frac{d\mathrm{dB}Z_{e\lambda}}{dr}. \tag{5}$$

Or expressing it in terms of θ_1 and θ_2, we obtain

$$\frac{d\mathrm{dB}Z_{m\lambda}}{dr} = -2k_\lambda(\theta_1, \theta_2) + \frac{\partial \mathrm{dB}Z_{e\lambda}}{\partial\theta_1}\frac{d\theta_1}{dr} + \frac{\partial \mathrm{dB}Z_{e\lambda}}{\partial\theta_2}\frac{d\theta_2}{dr}. \tag{6}$$

If we have radar reflectivity measurements at two frequency channels $\lambda = 1, 2$, then we have two equations of the form (6), and we get a simultaneous pair of differential equations for θ_1 and θ_2

$$\begin{pmatrix} \dfrac{d\theta_1(r)}{dr} \\ \dfrac{d\theta_2(r)}{dr} \end{pmatrix} = \mathcal{A}^{-1}\begin{pmatrix} \dfrac{d\mathrm{dB}Z_{m1}(r)}{dr} + 2k_1(\theta_1(r), \theta_2(r)) \\ \dfrac{d\mathrm{dB}Z_{m2}(r)}{dr} + 2k_2(\theta_1(r), \theta_2(r)) \end{pmatrix} \tag{7}$$

where

$$\mathcal{A} = \begin{pmatrix} \dfrac{\partial \mathrm{dB}Z_{e1}}{\partial\theta_1} & \dfrac{\partial \mathrm{dB}Z_{e1}}{\partial\theta_2} \\ \dfrac{\partial \mathrm{dB}Z_{e2}}{\partial\theta_1} & \dfrac{\partial \mathrm{dB}Z_{e2}}{\partial\theta_2} \end{pmatrix}. \tag{8}$$

The inverse of $\mathcal{A}$ is given by

$$\mathcal{A}^{-1} = \frac{1}{|\mathcal{A}|}\begin{pmatrix} \dfrac{\partial \mathrm{dB}Z_{e2}}{\partial\theta_2} & -\dfrac{\partial \mathrm{dB}Z_{e1}}{\partial\theta_2} \\ -\dfrac{\partial \mathrm{dB}Z_{e2}}{\partial\theta_1} & \dfrac{\partial \mathrm{dB}Z_{e1}}{\partial\theta_1} \end{pmatrix} \tag{9}$$

where $|\mathcal{A}|$ is the determinant of $\mathcal{A}$.

The PSD, $N(D)$, can be expressed as the product of the scale factor N_t and the normalized density function $p_n(D)$

$$N(D) = N_t\, p_n(D) \quad \text{where} \quad \int_D p_n(D)\,dD = 1. \tag{10}$$

We define M_i as the ith moment of $N(D)$

$$M_i = \int D^i N(D)\,dD. \tag{11}$$

To characterize the PSD by two parameters, they must be a combination of N_0 that is proportional to the total number density and a parameter that characterizes the distribution of $p_n(D)$. In this article, we choose

$$\theta_1 = 10\log_{10}(N_0), \quad \text{and} \tag{12}$$

$$\theta_2 = 10\log_{10}(D_m) \tag{13}$$

where both N_0 and D_m are defined individually by a combination of the third and fourth moments of $N(D)$ as

$$N_0 \overset{\text{def}}{=} \frac{M_3^5}{M_4^4} = N_t\frac{\left[\int D^3\, p_n(D)\,dD\right]^5}{\left[\int D^4\, p_n(D)\,dD\right]^4} \tag{14}$$

$$D_m \overset{\text{def}}{=} \frac{M_4}{M_3} = \frac{\int D^4\, p_n(D)\,dD}{\int D^3\, p_n(D)\,dD} \tag{15}$$

D_m is the volume weighted mean diameter, and N_0 is proportional to N_t. The intercept parameter N_w is related to N_0 by

$$N_w = \frac{128}{3} N_0. \tag{16}$$

Note that, in the case of ice particles, D_m derived from the equations in this article refers to the unmelted particle diameter whereas, in the operational data, D_m refers to the melted equivalent.

It is known that the natural variations of Z_e and k can generally be approximated well by functions of D_m for each wavelength once they are normalized by N_0 [6], [7]. In other words

$$\mathrm{dB}Z_{e\lambda} = \theta_1 + f_\lambda(\theta_2) \tag{17}$$

and

$$\mathrm{dB}k_\lambda = \theta_1 + g_\lambda(\theta_2). \tag{18}$$

Then, the matrix $\mathcal{A}$ and its inverse become

$$\mathcal{A} = \begin{pmatrix} 1 & f_1' \\ 1 & f_2' \end{pmatrix} \tag{19}$$

$$\mathcal{A}^{-1} = \frac{1}{f_2' - f_1'} \begin{pmatrix} f_2' & -f_1' \\ -1 & 1 \end{pmatrix} \tag{20}$$

where $f_\lambda' = df_\lambda/d\theta_2$.

Once a model PSD function is selected, we can calculate $f_\lambda(\theta_2)$, $g_\lambda(\theta_2)$, and their derivatives. Since $\mathrm{dB}Z_{m\lambda}(r)$ are measured at discrete ranges $r = r_i$ $(i = 1, \ldots, n)$, they can be used to solve the pair of differential equations (7) to obtain PSD parameters $\theta_1(r)$ and $\theta_2(r)$ numerically. Once these parameters are estimated, we can calculate the rainfall rate from them. This is the basic idea of retrieving two PSD parameters and estimating accurate rainfall rates from matched dual-wavelength radar data.

Unfortunately, however, there are a few problems associated with (7). They include a possible double-solution problem, instability of the solution, and no solution cases depending on the given data and the assumed PSD model.

It is worth noting here that (7) contains the measured data $\mathrm{dB}Z_{m,\lambda}$ by their derivatives only. As a result, constant biases in $\mathrm{dB}Z_{m,\lambda}$ are irrelevant as long as the initial conditions are properly given. In other words, calibration of echo power is important only in the process of determining the initial conditions.

B. Stability of the Solution

The solutions to the differential equation (7) are determined solely by the initial conditions. This fact indicates the importance of the selection of the initial conditions. If the initial conditions deviate from the true conditions, the obtained solutions may differ from the actual profiles of θ_1 and θ_2. Whether small deviations of the initial conditions from the true values increase with range or decrease to zero can be analyzed by looking at the stability of the system of equations for the difference of two sets of solutions to (7), which results from two initial conditions that differ by a small amount. More specifically, let the solution obtained from the initial condition $(\theta_{10}, \theta_{20})$ be $(\theta_1(r), \theta_2(r))$ and a nearby solution obtained from the initial condition $(\theta_{10} + \Delta\theta_{10}, \theta_{20} + \Delta\theta_{20})$ be $(\theta_1(r) + \Delta\theta_1(r), \theta_2(r) + \Delta\theta_2(r))$.

For small $(\Delta\theta_{10}, \Delta\theta_{20})$, the equation for $(\Delta\theta_1(r), \Delta\theta_2(r))$ can be obtained by taking the first-order terms of the Taylor expansion of (7) and be expressed in the matrix form as follows:

$$\frac{d}{dr}\begin{pmatrix} \Delta\theta_1 \\ \Delta\theta_2 \end{pmatrix} = \mathcal{B}\begin{pmatrix} \Delta\theta_1 \\ \Delta\theta_2 \end{pmatrix} = \begin{pmatrix} b_{11} & b_{12} \\ b_{21} & b_{22} \end{pmatrix}\begin{pmatrix} \Delta\theta_1 \\ \Delta\theta_2 \end{pmatrix}. \tag{21}$$

After some tedious calculations, the elements of $\mathcal{B}$ turn out to be

$$b_{11} = \frac{2q\left(f_1'k_2 - f_2'k_1\right)}{f_1' - f_2'} \tag{22}$$

$$b_{12} = \frac{2q\left(f_1'g_2'k_2 - f_2'g_1'k_1\right)}{f_1' - f_2'} - \frac{f_1'f_2'' - f_2'f_1''}{f_1' - f_2'}\frac{d\theta_2}{dr} \tag{23}$$

$$b_{21} = \frac{2q(k_1 - k_2)}{f_1' - f_2'} \tag{24}$$

$$b_{22} = \frac{2q\left(g_1'k_1 - g_2'k_2\right)}{f_1' - f_2'} - \frac{f_1'' - f_2''}{f_1' - f_2'}\frac{d\theta_2}{dr}. \tag{25}$$

A prime indicates differentiation with respect to θ_2.

The stability of (21) is determined by the trace and the determinant of the coefficient matrix $\mathcal{B}$ [8]. It is known that the stationary point, which is $\Delta\theta_1(r) = 0$ and $\Delta\theta_2(r) = 0$ in the current case, is a stable and convergent point (sink) if $\det\mathcal{B} > 0$ and $\mathrm{Tr}\,\mathcal{B} < 0$. If $\det\mathcal{B} > 0$ and $\mathrm{Tr}\,\mathcal{B} > 0$, it is an unstable and divergent point (source). If $\det\mathcal{B} < 0$, it is a saddle point and unstable.

In a case of uniform rain in which θ_1 and θ_2 do not depend on range r so that $d\theta_2/dr = 0$, the trace and determinant of $\mathcal{B}$ are

$$\mathrm{Tr}\,\mathcal{B} = \frac{2q}{f_1' - f_2'}\left(\left(f_1' - g_2'\right)k_2 - \left(f_2' - g_1'\right)k_1\right) \tag{26}$$

$$\det\mathcal{B} = \frac{4q^2k_1k_2\left(g_1' - g_2'\right)}{f_1' - f_2'}. \tag{27}$$

We define the dual-frequency ratio of specific attenuation, DFk, by

$$\mathrm{DFk} \overset{\mathrm{def}}{=} \frac{k_1}{k_2} = \frac{\exp(qg_1(\theta_2))}{\exp(qg_2(\theta_2))}. \tag{28}$$

DFk is a function of θ_2 alone similar to DFR. Note that $\mathrm{DFR}' = f_1' - f_2'$ and $\mathrm{DFk}' = q(k_1/k_2)(g_1' - g_2')$. Since $(f_1' - g_2')k_2 - (f_2' - g_1')k_1 > 0$, the sign of $\mathrm{Tr}\,\mathcal{B}$ depends only on the derivative of DFR with respect to θ_2. The sign of $\det\mathcal{B}$ is determined by $(g_1' - g_2')/(f_1' - f_2')$. DFR$'$ changes its sign from negative to positive at $\theta_2 = \theta_{2c}$ where θ_{2c} corresponds to the critical diameter D_{mc} at which DFR takes its minimum value. Similarly, $g_1' - g_2'$ changes its sign at the diameter D_{mk} at which DFk takes its minimum value. As a result, when D_m increases from 0, the sign of $\det\mathcal{B}$ changes from positive to negative at D_{mk} and then to positive again at D_{mc} if $D_{mk} < D_{mc}$.

Fig. 1 shows how DFR and DFk as functions of D_m change with the temperature and the shape factor μ of the gamma PSD for liquid water particles. D_{mc} at which DFR takes its minimum value changes with μ. Different temperatures do not change D_{mc} much but change the depth of the DFR curve.

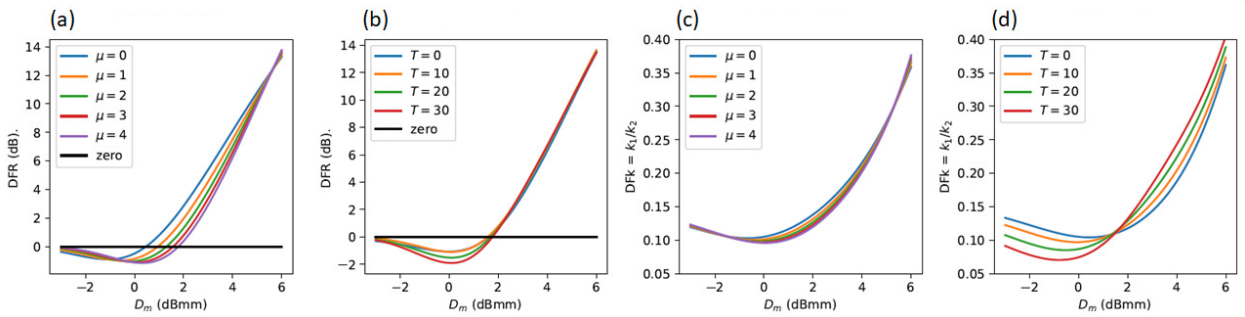

Fig. 1. Dependence of DFR and DFk on temperature and shape factor μ of spherical liquid water particles that follow the gamma PSD. (a) DFR, $T = 10$ °C. (b) DFR, $\mu = 3$. (c) DFK, $T = 10$ °C. (d) DFK, $\mu = 3$.

On the other hand, DFk is relatively insensitive to μ, but the depth and location of the minimum depend on the temperature. One other quantity of interest is D_{ms}, which is the value of D_m above which the inverse function of DFR(D_m) is single-valued. Fig. 2 shows how D_{mc}, D_{mk}, and D_{ms} change with μ for different temperatures.

In the uniform rain case, if we solve (7) backward, the sign of Tr $\mathcal{B}$ changes, but the sign of det $\mathcal{B}$ remains the same. From these observations, it can be said that the forward solution is stable only in the domain $D_m < \min(D_{mk}, D_{mc})$ and unstable in the domain $D_m > \min(D_{mk}, D_{mc})$, whereas the backward solution is stable in the domain $D_m > \max(D_{mk}, D_{mc})$ but unstable for $D_m < \max(D_{mk}, D_{mc})$. In the interval $[\min(D_{mk}, D_{mc}), \max(D_{mk}, D_{mc})]$, neither solution is stable (see Fig. 3). It is worthwhile to note that changing the parameters θ_1 and θ_2 to any other related pair of parameters does not change the stability because the linear transformation of infinitesimal parameters does not change the trace and determinant of the coefficient matrix after the transformation.

The mathematical theory of stability can be used to describe the behavior of solution for $r \to \infty$. For the radar problem, however, the range of r is finite. As a result, even if the solution were mathematically convergent, the actual solution obtained with arbitrary initial conditions would not necessarily converge over the finite range. This fact also implies that the solutions do not necessarily diverge from the true solution very rapidly in the cases in which the true solution is not a convergent point. The rate of convergence or divergence is rather complicated; examples of this can be found in Section IV.

The behavior of solutions near the stationary point can be analyzed by the eigenvalues and the corresponding eigenvectors. With a gamma PSD model, the two eigenvalues have a very large ratio of about 100 or more at all realistic values of D_m and N_0. This fact implies that the trajectory of the solution to a stationary point is actually nearly parallel to the eigenvector that corresponds to the larger eigenvalue and does not converge to the stationary point in practice. The trajectories of solutions are effectively the same as in the case with the determinant 0 so that the solution approaches a point on the line of stable fixed points of which direction is determined by the eigenvector for the smaller eigenvalue. Since the angle between these two eigenvectors is rather small, if the equation is solved from the initial values that deviate from the stationary solutions, because of the finite range, the solutions need not end at a stationary point, even in stable cases.

In the nonuniform rain case, because of the additional terms in b_{12} and b_{22}, the signs of both det $\mathcal{B}$ and Tr $\mathcal{B}$ depend not only on θ_2 but also on θ_1 and $d\theta_2/dr$. The additional terms are independent of θ_1, but the first terms in (23) and (25) are proportional to $N_0 (= \exp(q\theta_1))$ and change significantly with θ_1. As a result, even a very small deviation of $d\theta_2/dr$ from zero drastically changes the signs of det $\mathcal{B}$ and Tr $\mathcal{B}$ for a relatively small θ_1. In fact, a gradient of $d\theta_2/dr = \pm 0.1$ dB/km is large enough to modify the original domain of convergence in the uniform case. Fig. 3 shows the stable domains for both forward processing and backward processing when $d\theta_2/dr = 0, +0.1$, and -0.1 dB/km. It can be said that, in forward processing, the stable domain shrinks when there is a gradient in θ_2 regardless of its sign. However, the stable domain increases in the backward processing by adding a new stable region in the negative θ_2 domain when $d\theta_2/dr < 0$ for relatively small θ_2. It can be seen in (23) and (25) that, if $d\theta_2/dr$ and k_λ increase by the same factor, the dependence of the signs of det $\mathcal{B}$ and Tr $\mathcal{B}$ on θ_2 remains the same. In other words, if $d\theta_2/dr$ increases by a factor of a and θ_1 increases by $10\log_{10}(a)$, the whole patterns in Fig. 3 shift vertically along the N_w axis by $10\log_{10}(a)$, and their dependence on θ_2 does not change. For example, if $d\theta_2/dr$ changes from 0.1 to 1 dB/km, the patterns in Fig. 3(b) and (c) shift upward by 10 dB. Note that the stability does not depend on $d\theta_1/dr$, i.e., the gradient of N_0 does not affect the stability.

Although the boundaries of the stable domains change by the gradient of θ_2, the direction of the eigenvector for the larger eigenvalue remains effectively the same, and the absolute value of the smaller eigenvalue is always very close to 0. Because of these properties, the convergence and divergence patterns of $\Delta\theta_1$ and $\Delta\theta_2$ in the nonuniform case are similar to those in the uniform case. The eigenvalues of the matrix $\mathcal{B}$ determine the convergent and divergent rates of $\Delta\theta$ per unit distance. Areas with a positive eigenvalue correspond to a diverging area, i.e., the area in which the error in the initial conditions increases with the processing distance. If we accept as a practically stable domain a small eigenvalue area in which the error increases only moderately, the practically stable domain increases substantially. For example, the area with the larger eigenvalue less than q corresponds to the domain

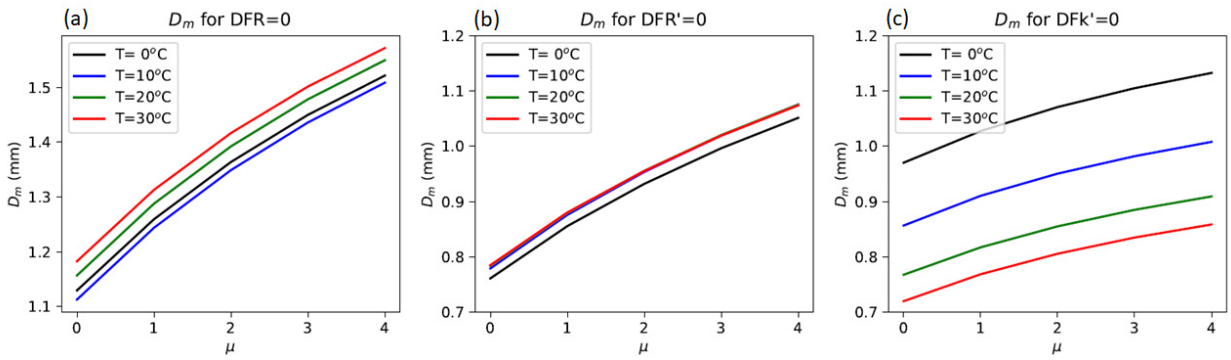

Fig. 2. Temperature and μ dependence of D_m at which (a) DFR = 0, (b) DFR' = 0, and (c) DFk' = 0 for spherical liquid water particles whose PSD follows the gamma distribution. They correspond to D_{ms}, D_{mc}, and D_{mk}, respectively.

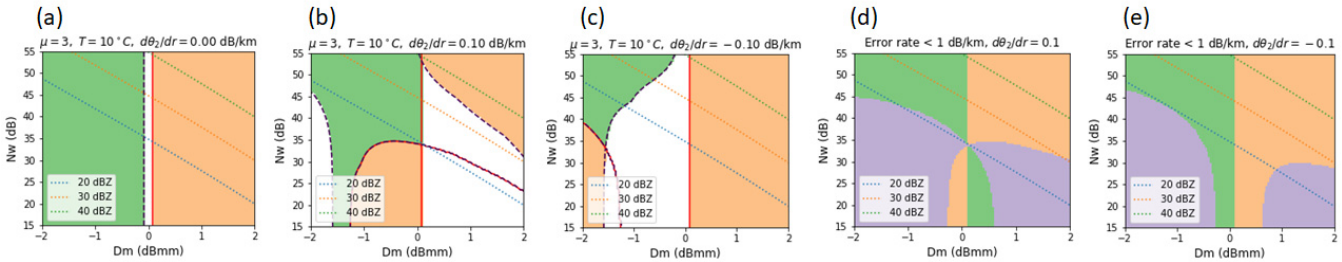

Fig. 3. Stability and error diagrams for $\mu = 3$ and $T = 10$ °C for liquid water particles. The green and orange areas indicate stable regions for forward processing and backward processing, respectively, in (a)–(c). Neither processing is stable in the white area. The red lines show the locations where the first eigenvalue changes its sign, whereas the dashed lines show those of the second eigenvalue. The vertical red line near $D_m = 0$ dBmm corresponds to D_{mc} at which DFR takes its minimum value. The stable regions correspond to the area in which the real parts of both eigenvalues are negative. (a) Uniform rain case, i.e., $d\theta_2/dr = 0.0$ dB/km. (b) D_m increases with range at a rate of $d\theta_2/dr = 0.1$ dB/km. (c) D_m decreases with range at a rate of $d\theta_2/dr = -0.1$ dB/km. (d) and (e) Regions with the error increasing rate less than 26% per km in the cases of (b) and (c), respectively. The purple areas indicate the areas in which both forward processing and backward processing satisfy the error condition. Dotted lines show the equi-dBZ_e lines at the Ku-band.

in which the increase in the error rate is less than 1 dB/km (≡26%/km). The area defined by this condition shares most of the practically important part (dBZ_e(Ku) > 20 dBZ) of the stable domain in the uniform rain case. Fig. 3(d) and (e) show such examples. All these properties of the differential equation (7) are applicable to the discrete equations that will be discussed in the remaining sections.

It is easy to understand that (7) has a singular point at $D_m = D_{mc}$ because $\mathcal{A}^{-1}$ has $f_1' - f_2'$ in the denominator, which makes $\mathcal{A}^{-1}$ diverge at $D_m = D_{mc}$. Since the right-hand side of (7) is discontinuous at $D_m = D_{mc}$, there is no continuous solution of θ_2 that crosses the boundary at $D_m = D_{mc}$. The solution diverges when it hits this boundary. To cross this boundary, we need to use a discretized system of equations with a finite range step. The double value problem and the no-solution issue will be discussed for such discretized equations in the next section.

III. Discretized Equation

A new discretized system of equations is proposed in this section. Instead of discretizing the differential equation (7) by approximating it by finite steps in r, we start with (2). We derive a set of equations that relate the PSD parameters in a range bin to those in the adjacent bin. Once such equations are found and if a set of initial conditions are given properly, we can calculate the PSD parameters at all bins.

We assume that the measured data are available only at discrete range bins: $r = r_i$ $(i = 1, \ldots, n, n \in N)$. r_1 is the range to the center of the first range bin in which the precipitation echo starts. We introduce the following notation:

$$\mathrm{dB}Z_{m\lambda,i} \stackrel{\mathrm{def}}{=} \mathrm{dB}Z_{m\lambda}(r_i) \tag{29}$$

$$\mathrm{dB}Z_{e\lambda,i} \stackrel{\mathrm{def}}{=} \mathrm{dB}Z_{e\lambda}(r_i) \tag{30}$$

$$k_{\lambda,i} \stackrel{\mathrm{def}}{=} k_\lambda(r_i) \tag{31}$$

$$A_{\lambda,i} \stackrel{\mathrm{def}}{=} 2\int_{r_0}^{r_i} k_\lambda(s)\,ds \tag{32}$$

$$\mathrm{DFRm}_i \stackrel{\mathrm{def}}{=} \mathrm{dB}Z_{m1,i} - \mathrm{dB}Z_{m2,i} \tag{33}$$

and

$$\Delta r = r_{i+1} - r_i, \quad (i = 1, \ldots, n-1). \tag{34}$$

Here, $A_{\lambda,i}$ is the two-way attenuation to range r_i at wavelength λ. With these notations, (2) becomes

$$\mathrm{dB}Z_{m\lambda,i} = \mathrm{dB}Z_{e\lambda,i} - A_{\lambda,i}, \qquad (\lambda = 1, 2). \tag{35}$$

We assume that we can approximate the attenuation between two adjacent bins by the average of the specific attenuations at the centers of these bins multiplied by twice the distance between them, that is,

$$A_{\lambda,i} - A_{\lambda,i-1} = 2\int_{r_{i-1}}^{r_i} k_\lambda(s)\,ds \tag{36}$$

$$\approx \Delta r\,(k_{\lambda,i} + k_{\lambda,i-1}). \tag{37}$$

Then, by taking the difference of (35) at $r = r_i$ and $r = r_{i-1}$, and rearranging the terms, we obtain

$$\mathrm{dB}Z_{e\lambda,i} - \Delta r\, k_{\lambda,i} = C_{\lambda,i}, \quad (\lambda = 1, 2) \tag{38}$$

where

$$C_{\lambda,i} = (\mathrm{dB}Z_{m\lambda,i} - \mathrm{dB}Z_{m\lambda,i-1}) + \mathrm{dB}Z_{e\lambda,i-1} + \Delta r\, k_{\lambda,i-1}. \tag{39}$$

A. Forward Equation

Taking the difference of the two equations for $\lambda = 1$ and $\lambda = 2$ in (38), we obtain

$$\mathrm{DFR}(\theta_{2,i}) + \Delta r\, k_{2,i}(1 - \mathrm{DFk}(\theta_{2,i})) = C_{1,i} - C_{2,i}. \tag{40}$$

Taking the ratio of $k_{1,i}$ to $k_{2,i}$ in (38), we obtain

$$\mathrm{dB}Z_{e1,i} - C_{1,i} = \mathrm{DFk}(\theta_{2,i})\,(\mathrm{dB}Z_{e2,i} - C_{2,i}). \tag{41}$$

The substitution of (17) into (41) gives

$$\theta_{1,i} + f_1(\theta_{2,i}) - C_{1,i} = \mathrm{DFk}(\theta_{2,i})\,(\theta_{1,i} + f_2(\theta_{2,i}) - C_{2,i}). \tag{42}$$

From (42), $\theta_{1,i}$ can be expressed as a function of $\theta_{2,i}$ as

$$\theta_{1,i} = -\frac{f_1(\theta_{2,i}) - f_2(\theta_{2,i})\,\mathrm{DFk}(\theta_{2,i})}{1 - \mathrm{DFk}(\theta_{2,i})} + \frac{C_{1,i} - C_{2,i}\,\mathrm{DFk}(\theta_{2,i})}{1 - \mathrm{DFk}(\theta_{2,i})}. \tag{43}$$

Similarly, the substitution of (18) into (40) gives

$$\mathrm{DFR}(\theta_{2,i}) + \Delta r \exp(q(\theta_{1,i} + g_2(\theta_{2,i})))(1 - \mathrm{DFk}(\theta_{2,i})) = C_{1,i} - C_{2,i}. \tag{44}$$

Equations (43) and (44) together with equations in (39) constitute the equations for $\theta_{1,i}$ and $\theta_{2,i}$:

Substitution of $\theta_{1,i}$ expressed in terms of $\theta_{2,i}$ in (43) into (44) gives a single equation for $\theta_{2,i}$ for given $C_{1,i}$ and $C_{2,i}$. Once this equation is solved for $\theta_{2,i}$, $\theta_{1,i}$ can be calculated by (43). Since $C_{1,i}$ and $C_{2,i}$ are given by the measured data and the PSD parameters at r_{i-1}, the PSD parameters at r_i can be obtained by solving (44) and (43). By repeating this procedure for all i from $i = 1$, we can estimate the PSD parameters at all range bins.

B. Backward Equation

By following exactly the same procedure as in the derivation of the forward equation, we can derive the backward equations.

The backward equations for $\theta_{1,i}$ and $\theta_{2,i}$ are

$$\theta_{1,i} = -\frac{f_1(\theta_{2,i}) - f_2(\theta_{2,i})\,\mathrm{DFk}(\theta_{2,i})}{1 - \mathrm{DFk}(\theta_{2,i})} + \frac{B_{1,i} - B_{2,i}\,\mathrm{DFk}(\theta_{2,i})}{1 - \mathrm{DFk}(\theta_{2,i})} \tag{45}$$

$$\mathrm{DFR}(\theta_{2,i}) - \Delta r \exp(q(\theta_{1,i} + g_2(\theta_{2,i})))(1 - \mathrm{DFk}(\theta_{2,i})) = B_{1,i} - B_{2,i}. \tag{46}$$

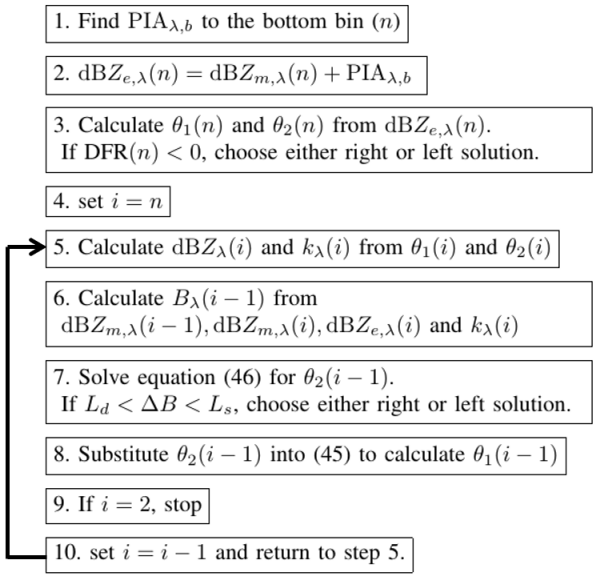

Fig. 4. Flowchart of the backward processing. The initial values of $\theta_1(n)$ and $\theta_2(n)$ must be given by some means. A case with the use of PIA$_{\lambda,b}$ is shown in the figure. Note that $\theta_1 = 10\log_{10} N_0$, $\theta_2 = 10\log_{10} D_m$, $\lambda = 1, 2$, and $\Delta B = B_1 - B_2$. L_d and L_s are defined in Fig. 7.

with

$$B_{\lambda,i} = (\mathrm{dB}Z_{m\lambda,i} - \mathrm{dB}Z_{m\lambda,i+1}) + \mathrm{dB}Z_{e\lambda,i+1} - \Delta r\, k_{\lambda,i+1}. \tag{47}$$

Equations (45) and (46) are identical to (43) and (44) except that the sign of Δr is reversed, and $C_{1,i}$ and $C_{2,i}$ are replaced by $B_{1,i}$ and $B_{2,i}$. $B_{1,i}$ and $B_{2,i}$ can be obtained from $C_{1,i}$ and $C_{2,i}$ by replacing subscript $i-1$ by $i+1$ and by changing the sign of Δr.

A simplified flowchart of the backward processing is shown in Fig. 4.

IV. Basic Properties of the Algorithm

Since $\mathrm{dB}Z_{m\lambda,i}$ is given at all i $(i = 1, \ldots, n)$ for both $\lambda = 1, 2$, if $\theta_{1,i-1}$ and $\theta_{2,i-1}$ are known, we can calculate $\mathrm{dB}Z_{e\lambda,i-1}$ and $k_{\lambda,i-1}$, and hence, $C_{1,i}$ and $C_{2,i}$ as well. Similarly, if $\theta_{1,i+1}$ and $\theta_{2,i+1}$ are known, we can calculate $B_{1,i}$ and $B_{2,i}$. Substitution of (43) into (44) gives the forward equation of $\theta_{2,i}$ for given $C_{1,i}$ and $C_{2,i}$, and substitution of (45) into (46) gives the backward equation of $\theta_{2,i}$ for given $B_{1,i}$ and $B_{2,i}$. In either case, the equations depend only on two parameters $C_{1,i}$ and $C_{2,i}$, or $B_{1,i}$ and $B_{2,i}$ which contains the difference of $\mathrm{dB}Z_{m\lambda,i}$ between two adjacent range bins. As a result, the solutions only depend on the initial conditions and the slope of $\mathrm{dB}Z_{m\lambda,i}$ and do not depend on the absolute values of $\mathrm{dB}Z_{m\lambda,i}$. This property is common with the differential form of equations mentioned in Section II.

Both the forward and backward equations are basically derived from equation (37) together with (35), which can be rewritten as

$$A_{\lambda,i-1} + \Delta r\, k_{\lambda,i-1} = A_{\lambda,i} - \Delta r\, k_{\lambda,i}, \quad (\lambda = 1, 2). \tag{48}$$

Both sides of this equation give the attenuation estimate at the midpoint between ranges r_{i-1} and r_i, i.e., at $r = r_{i-1} + \Delta r/2 = r_i - \Delta r/2$. In other words, this equation gives the condition that the attenuation calculated forward from the bin center of bin $i-1$ and that backward from the bin center of bin i should agree at each frequency.

A. Double-Value Problem

This method does not solve the problem of dual solutions. In fact, the number of the solutions of (44) or (46) changes with the value of $C_{1,i}$ and $C_{2,i}$ or $B_{1,i}$ and $B_{2,i}$. To explain how the number of solutions changes, we define the left-hand side of the forward equation (44) as $L_F(\theta_2; C_1, C_2)$ or simply $L_F(\theta_2)$ and the left-hand side of the backward equation (46) as $L_B(\theta_2; B_1, B_2)$ or simply $L_B(\theta_2)$ after substituting θ_1 of (43) and (45) into θ_1 in (44) and (46), respectively. When we do not need to distinguish $L_F(\theta_2)$ and $L_B(\theta_2)$, we simply write $L(\theta_2)$ for brevity. The subscript i is omitted below because the equations hold for an arbitrary range bin. Because of the smallness of the factor $\mathrm{DFk}(\theta_2)$ in (43) and (45), $L_F(\theta_2)$ ($L_B(\theta_2)$) depends much more on C_1 (B_1) than on C_2 (B_2). In other words, $L_F(\theta_2)$ ($L_B(\theta_2)$) depends much more on the Ku-band than the Ka-band data.

Fig. 5 shows how $L_F(\theta_2; C_1, C_2)$ ($L_B(\theta_2; B_1, B_2)$) changes with various values of $\mathrm{dB}Z_e(\mathrm{Ku})$ when true $\theta_2 = -1$ (dBmm) and $\Delta r = 1$ km. C_1, C_2, B_1, and B_2 are calculated from $\mathrm{dB}Z_e(\mathrm{Ku})$ and the given conditions. Note that C_1 and B_1 are approximately equal to $\mathrm{dB}Z_e(\mathrm{Ku})$. As can be seen from the results, the domain of double solutions of θ_2 increases with $\mathrm{dB}Z_e(\mathrm{Ku})$ for $L_F(\theta_2)$ but decreases with $\mathrm{dB}Z_e(\mathrm{Ku})$ for $L_B(\theta_2)$. When $\mathrm{dB}Z_e(\mathrm{Ku})$ is sufficiently large, $L_B(\theta_2)$ becomes a monotonically increasing function of θ_2 so that the double-solution problem disappears. This property can be explained as follows. Equation (45) gives θ_1 as a function of θ_2. Its dependence on θ_2 is predominantly determined by $f_1(\theta_2)$. Since the slope of $f_1(\theta_2)$ is larger than that of $g_2(\theta_2)$, $\theta_1(\theta_2) + g_2(\theta_2)$ in (46) increases with decreasing θ_2 for small θ_2 as $\theta_2 \to -\infty$ [note the minus sign in front of $f_1(\theta_2)$ in (45)]. This dependence of $\theta_1(\theta_2) + g_2(\theta_2)$ on θ_2 contributes an exponential increase in the attenuation term in $L_B(\theta_2)$ when $\theta_2 \to -\infty$. If $\mathrm{dB}Z_e(\mathrm{Ku})$ is large, θ_1 itself becomes large through $B_{1,i}$ in (45), and hence, the contribution of the positive slope from the second term in $L_B(\theta_2)$ overwhelms the negative slope of $\mathrm{DFR}(\theta_2)$ for small θ_2.

On the other hand, the domain of dual solutions increases with increasing C_1 in the forward processing. Fig. 6 shows how the number of solutions depends on the combination of C_1 and C_2 or B_1 and B_2 when $\Delta r = 1$ km. Note that the value of C_1 (or B_1) is close to $Z_e(\mathrm{Ku})$ because both $\mathrm{dB}Z_{m1,i} - \mathrm{dB}Z_{m1,i-1}$ (or $\mathrm{dB}Z_{m1,i} - \mathrm{dB}Z_{m1,i+1}$) and the attenuation within the bin are generally small. The number of solutions shown in Fig. 6 is the solution within the interval of $[-3, 6]$ for θ_2. The no solution region in the lower right corner of the graph comes from the upper limit of $\theta_2 = 6$. The right-hand boundary between single and double solutions in the forward processing changes with the lower limit of the allowable domain of θ_2.

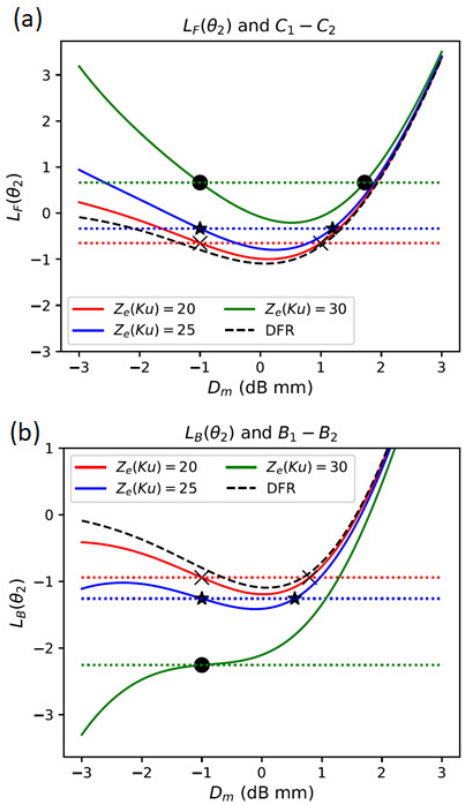

Fig. 5. (a) Function $L_F(\theta_2; C_1, C_2)$ for true $\mathrm{dB}Z_e(\mathrm{Ku}) = 20, 25, 30$ dB, $\mathrm{dB}D_m = -1$, and $\Delta r = 1$ km. $C_1 - C_2$ shown by a dotted line becomes -0.65, -0.33, and 0.66, respectively. (b) Function $L_B(\theta_2; B_1, B_2)$ for $\mathrm{dB}Z_e(\mathrm{Ku}) = 20, 25, 30$ dB, $\mathrm{dB}D_m = -1$, and $\Delta r = 1$ km. $B_1 - B_2$ becomes -0.94, -1.26, and -2.26, respectively. Note that $\theta_2 = 10\log_{10}(D_m)$.

The graph of $L_B(\theta_2)$ shows that the equation $L_B(\theta_2; B_1, B_2) = B_1 - B_2$ may have up to three solutions because $L_B(\theta_2)$ goes to $-\infty$ as θ_2 goes to $-\infty$. However, in order to avoid unrealistic solutions, the searching domain of the solutions is limited within the interval $[\theta_{2,l}, \theta_{2,u}]$. In the examples shown later in this article, we choose the lower limit $\theta_{2,l} = -2$ and the upper limit $\theta_{2,u} = 6$. These numbers correspond to $D_m = 0.63$ mm and $D_m = 4.0$ mm. Within this searching domain, the number of solutions is 0, 1, or 2 depending on the values of C_1 and C_2 in the forward processing, and B_1 and B_2 in the backward processing.

Let us define L_d as the minimum value of $L(\theta_2)$ for $\theta_2 \in [\theta_{2,l}, \theta_{2,u}]$ and $\theta_{2,d}$ as the value of θ_2 that makes $L(\theta_{2,d}) = L_d$ (see Fig. 7). We also define L_s as the value of $L(\theta_2)$ above which the inverse function has a single solution and $\theta_{2,s}$ as the corresponding diameter: $L(\theta_{2,s}) = L_s$. Similarly, we define $L_l = L(\theta_{2,l})$ and $L_u = L(\theta_{2,u})$. $L_s = L_l$ but $\theta_{2,l} \neq \theta_{2,s}$ in general. However, note that $\theta_{2,l} = \theta_{2,d} = \theta_{2,s}$ and $L_l = L_d = L_s$ when B_1 is sufficiently large and $L(\theta_2)$ is a monotonically increasing function over $[\theta_{2,l}, \theta_{2,u}]$.

We take $\theta_{2,l}$ large enough so that $L_l < L_u$ even if the attenuation within a bin is very large in the forward processing. Under this condition, we can define four possible cases. Let us define $\Delta C = C_1 - C_2$ and $\Delta B = B_1 - B_2$. Then, these four cases are categorized by the interval in which ΔC or ΔB

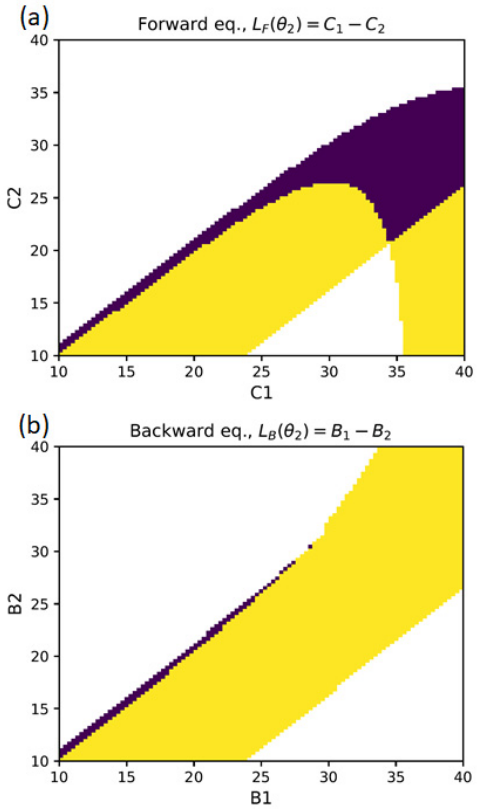

Fig. 6. (a) Number of solutions in (44): $L_F(\theta_2) = C_1 - C_2$ for $\Delta r = 1$ km. (b) Number of solutions in (46): $L_B(\theta_2) = B_1 - B_2$ for $\Delta r = 1$ km. Dark shaded areas have two solutions, and light-shaded areas have a single solution.

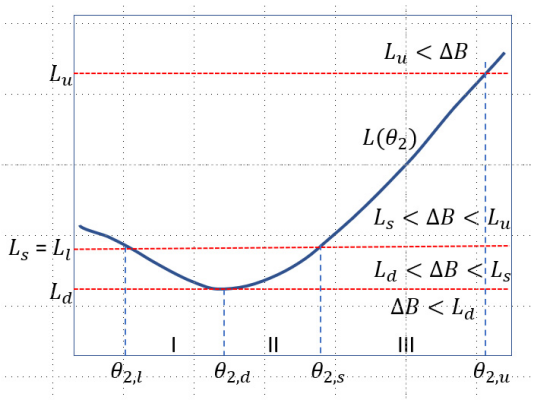

Fig. 7. Definitions of L_l, L_d, L_s, L_u, $\theta_{2,l}$, $\theta_{2,d}$, $\theta_{2,s}$, $\theta_{2,u}$, and domains I, II, and III.

falls: $[-\infty, L_d]$, $[L_d, L_s]$, $[L_s, L_u]$, or $[L_u, +\infty]$. We label the interval $[\theta_{2,l}, \theta_{2,d}]$ domain I, $[\theta_{2,d}, \theta_{2,s}]$ domain II, and $[\theta_{2,s}, \theta_{2,u}]$ domain III. Note that $\theta_{2,d} \approx 0$ and $\theta_{2,s} \approx 1$ in the case of $\mu = 3$ correspond to values of D_m of 1 mm, and 1.26 mm, respectively, and are fairly typical values of D_m for light to moderate rain rates.

When ΔB is between L_d and L_s, two solutions are possible; one in domain I, the left-hand side solution, and the other in domain II, the right-hand side solution. Both solutions satisfy the equation, but they give different estimates of $Z_{e\lambda}$ and k_λ for the following adjacent range bin.

When $\Delta B = B_1 - B_2$ (or $\Delta C = C_1 - C_2$) is less than L_d, there is no solution to (46) [or (44)]. In this case, the obvious choice of the solution is $\theta_{2,d}$. However, $\theta_{2,d}$ does not satisfy the equation. The difference $L_B(\theta_{2,d}) - \Delta B$ (or $L_F(\theta_{2,d}) - \Delta C$) must be accounted for the calculation for the next range bin. Without this correction, the residual error accumulates and the retrieved estimates of the PSD parameters no longer reproduce the measured profiles of $Z_{m\lambda}$ ($\lambda = 1, 2$). In practice, the difference $L_B(\theta_{2,d}) - \Delta B$ is subtracted from B_2 in the next step. This compensation method effectively attributes the difference to the Ka-band measured reflectivity factor, Z_{m2}, and ignores the weak dependence of $L_B(\theta_2)$ on B_2. The same correction is applied when there is no solution when $\Delta B > L_u$.

In the ice region, the DFR is always positive and approaches monotonically and asymptotically 0 dB as D_m decreases. In this case, $\theta_{2,l} = \theta_{2,d} = \theta_{2,s}$, and domains I and II disappear. If the measured data give $\Delta B < L_l \approx 0$, the best choice without any constraint would be $\theta_2 = -\infty$ or $D_m = 0$. However, a small value of D_m or a large negative value of $\theta_2 (=\mathrm{dB}D_m)$ gives a huge estimate of θ_1 $(=\mathrm{dB}N_0)$. This large estimate of θ_1 often causes an overflow in the computation of k in which θ_1 appears in the exponent. To avoid this practical problem, we need to define a reasonable minimum allowable D_m or $\theta_{2,l}$. The need for setting a minimum allowable $\theta_{2,l}$ is also applicable to the liquid precipitation.

In contrast to the backward processing, the dual-solution domain of θ_2 increases as the attenuation within the range bin increases in the forward processing. However, since the forward processing is applied only in the solid precipitation region in which the attenuation can be ignored, and since DFR is a monotonic function of D_m for solid precipitation, the dual-solution problem does not occur.

The double-value problem is mitigated with the backward processing when the attenuation between adjacent bins is large. To make $L_B(\theta_2)$ a monotonically increasing function of θ_2, the attenuation term $\Delta r k_2$ in (46) needs to be at least one dB. For the DPR, $\mathrm{dB}Z_{m,\lambda}$ is available at range intervals of 0.125 km. With this sampling interval of Δr, k_2 must be larger than a few dB/km. Such a large attenuation cannot be expected in light rain. In actual situations, large attenuations appear only in rather heavy rain. Such heavy rain is generally associated with large D_m at which DFR is positive so that the mitigation of the double-solution issue by the proposed algorithm is not effective as long as small Δr is used. Increasing Δr will increase the attenuation term and, hence, the single solution cases. The feasibility of this approach is discussed in the discussion section.

B. Stability

To examine the stability of the solution for the discretized equations (44) and (46), we assume a uniform rain field in which the true $Z_{e\lambda,i}$ and $k_{\lambda,i}$ are constant, or equivalently, $\theta_{1,i}$ and $\theta_{2,i}$ are constant. Equation (44) for a uniform case ($\theta_1 = \theta_{1,i} = \theta_{1,i-1}$ and $\theta_2 = \theta_{2,i} = \theta_{2,i-1}$) becomes

$$\exp(q(\theta_1 + g_2(\theta_2)) - \exp(q(\theta_1 + g_1(\theta_2)) = \frac{\Delta \mathrm{DFRm}}{2\Delta r} \quad (49)$$

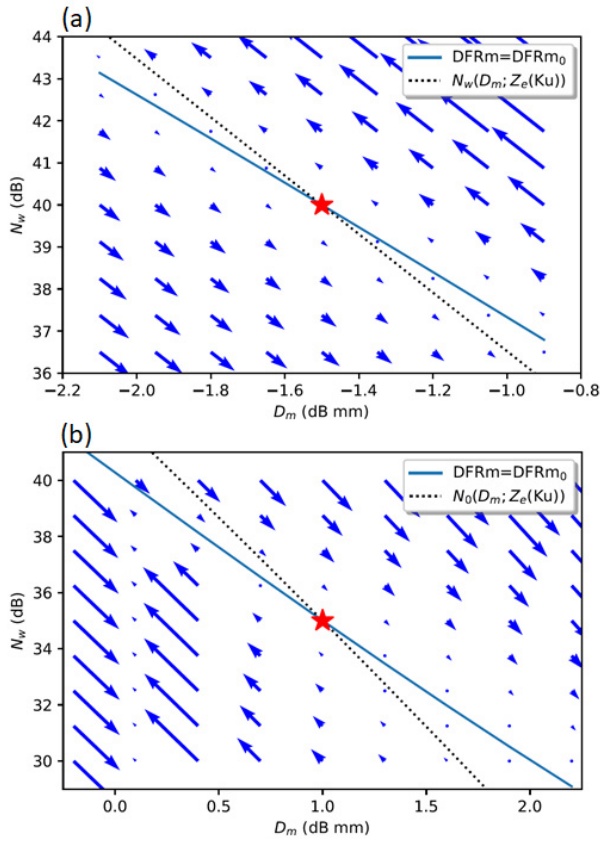

Fig. 8. Flow from $(\theta_{2,i+1}, \theta_{1,i+1})$ to $(\theta_{2,i}, \theta_{1,i})$ in the backward processing with $\Delta r = 0.125$ km when the true solution which is shown by the red star is $(-1.5, 40)$ for domain I (a) and $(1.0, 35)$ for domain II or III (b). The solid lines indicate the stationary solution line defined by (50). The dotted lines show N_w for the given Z_e(Ku).

where $\Delta\text{DFRm} = \text{DFRm}_i - \text{DFRm}_{i-1}$. Thus, the stationary solution lies on the line defined by the following equation:

$$\theta_1 = \frac{1}{q}\ln\left(\frac{\Delta\text{DFRm}}{2\Delta r}\right) - \frac{1}{q}\ln[\exp(qg_2(\theta_2)) - \exp(qg_1(\theta_2))]. \quad (50)$$

The true solution is on this line, but it may not be reached from any initial point in finite steps.

Fig. 8 shows the flow of the solutions in one step with $\Delta r = 0.125$ km from various initial points in the D_m-N_w space in the backward processing. The base of each arrow is the starting point, and its tip indicates the solution in the following bin. The directions of arrows are nearly parallel to the line defined by $\theta_1 = \text{dB}Z_e(\text{Ku}) - f_1(\theta_2)$. Their magnitude decreases as the initial point approaches the stationary solution line defined by (50). Since these two lines cross each other with a small angle, convergence to (or divergence from) the true solution is not apparent. The solutions remain close to the stationary line without approaching the true solution. A closer look reveals that, in the unstable case [see Fig. 8(a)], arrows are directed away from the stationary solution line, While, in the stable case [see Fig. 8(b)], they are directed toward the stationary solution line as long as the initial points are not far from the true stationary solution. If the initial point is far from the stationary line, the solution after a final step may end up at a point separated substantially from the true solution. As mentioned in Section II, since the ratio of the absolute values of the two eigenvalues is very large, a stable solution tends to converge to a point on the stationary line, which is not necessarily close to the true solution. These characteristics imply that the selection of the initial conditions is very important. For example, in the case shown in Fig. 8(b), the true stationary point is $\theta_2 = 1.0$ and $N_w = 35$. If the initial values of $\theta_2 = 1.2$ and $N_w = 37$ are given, the solutions converge to about $\theta_2 = 2.0$ and $N_w = 30$ after 50 steps ($\approx$6 km). The value of N_w is expressed in dB with units of $\text{m}^{-3}\text{mm}^{-1}$. Note, however, that this solution reproduces exactly the same $\text{dB}Z_{m,\lambda}$ slopes with the measured profiles of $\text{dB}Z_{m,\lambda}$, but their absolute values are biased. The reproduced $\text{dB}Z_{e,\lambda}$ values are biased as well.

Nevertheless, if the appropriate initial conditions are properly selected so that they do not cause any significant biases in the estimates of $\text{dB}Z_{e,\lambda}$, all such solutions satisfy the attenuation condition given by (37). This attenuation difference is mainly determined by the Ka-band attenuation. Since the attenuation in the Ka-band is highly correlated with the rainfall rate irrespective of the PSD, the estimate of R is generally close to the true value even if N_0 and D_m estimates are not close to the true values in the convergent region as long as the total path attenuation is properly given.

The solution from the forward method often gives an unrealistic profile in ranges where the attenuation becomes significant. Nevertheless, when the total path attenuation remains small, the forward method gives rather reasonable profiles. This is the case for snow profiling above the bright band in stratiform rain.

In a solid precipitation region in which the attenuation due to both scattering and absorption is small, we can assume that the attenuations are negligible. In such a case, (44) degenerates to $\text{DFR}(\theta_{2,i}) = \text{DFRm}_i$. Then, the D_m estimates are determined mostly by measured reflectivity factors that are nearly identical to the true effective reflectivity factors. The solutions of PSD parameters in such a region by the forward method effectively depend only on the assumed PSD and scattering models.

This fact can be verified by comparing D_m estimated by the forward method with the corresponding D_m directly calculated from DFRm. Fig. 9(a) and (b) shows the estimated D_m at 7 km above the sea level from the forward method and DFRm measured from the DPR data obtained from orbit 31343, scans 2650$\sim$2749 in the vicinity of hurricane Dorian on September 4, 2019. The agreement is generally very good. Fig. 9(c) shows the averages of D_m profiles from the Dorian case. The estimated average D_m profiles from DFRm and the forward processing method are effectively identical. Such an agreement is almost always the case in ice precipitation regions above the bright band in stratiform rain.

Even in ice precipitation, discrepancies appear when the measured radar reflectivity factor $\text{dB}Z_m$ is significant. In such a case, even though the absorption by ice particles is negligible, the attenuation due to scattering causes the difference

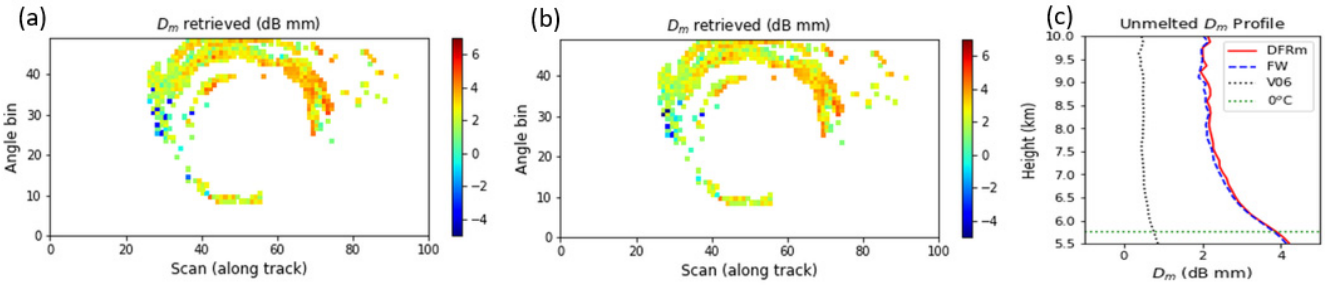

Fig. 9. Estimated D_m at 7 km above the sea level from (a) forward method and (b) from DFRm. (c) Averaged profile of D_m from all profiles in 100 scans that satisfy the condition of processing that $\mathrm{dB}Z_m$(Ka) is larger than 20 dBZ for at least ten consecutive range bins (1.25 km). DPR data are from orbit 31343, scan 2650–2749 in the vicinity of hurricane Dorian. D_m is unmelted mean diameter expressed in dB scale in mm. $\rho = 0.2$ g/mm^3 is assumed. D_m from V06X is melted mean diameter.

between $\mathrm{dB}Z_m$ and $\mathrm{dB}Z_e$ because of the existence of large particles. Since the PSD of such particles may differ from the assumed PSD, the D_m estimates may have large biases. In a heavy convective storm, there may be wet hail stones that further complicate the problem.

C. Initial Conditions

The convergence property of the algorithm mentioned in Section II-B implies the importance of the initial conditions. In the case of forward processing, we can safely assume that the attenuation to the first range gate is negligible and regard Z_m as Z_e at both frequencies at the storm top provided that the radar is well calibrated. In this case, we can equate DFRm and DFR from which D_m can be estimated there. N_0 can be calculated from $Z_m(\approx Z_e)$ and D_m provided that we know the phase state and density of the particles in the case of solid precipitation. In the case of liquid precipitation, we may encounter the double-solution issue.

In the case of backward processing, we need to specify $B_{1,i}$ and $B_{2,i}$ at the farthest range. To do so is equivalent to specifying the pair D_m and N_0 from which we can calculate Z_{e1}, Z_{e2}, k_1, and k_2, and hence, $B_{1,i}$ and $B_{2,i}$. Instead of D_m and N_0, we can also use the attenuation estimates to the bottom range since Z_{e1} and Z_{e2} can be obtained from Z_{m1} and Z_{m2} if the attenuations are known. Once Z_{e1} and Z_{e2} are given, we can calculate D_m and N_0 and then k_1 and k_2 from them. In particular, if the PIAs to the surface at the two frequencies are known, we can use them to specify the initial values of $B_{1,i}$ and $B_{2,i}$. Appendix A gives a formula that specifies the initial conditions by the PIA to the surface when there is some unobservable range between the clutter-free bottom and the surface under the condition that Z_e's at both frequencies are constant there.

In addition to the SRT that gives the PIA estimates, however, a different method is examined to specify the initial conditions in order to investigate possible biases that may exist in the SRT's PIA estimates. In particular, when rain is light, the relative errors in the PIA estimates by the SRT become rather large because their absolute values may be comparable to the fluctuation of surface echoes.

One promising method that is similar to the one used in the operational algorithm is given as follows [5]. First, assume a power law k_1–Z_{e1} relation for the Ku-band as $k_1 = \alpha Z_{e1}^{\beta}$ where β is a fixed constant. Use the Hitschfeld–Bordan (HB) method [9], [10] to estimate the attenuation corrected $Z_{e1}(r_i;\alpha)$ profile of the Ku-band that depends on the adjustable constant α. Since the assumed k_1–Z_{e1} relation defines the relation between D_m ($\equiv \theta_2$) and N_0 ($\equiv \theta_1$), as described in the first box in Fig. 10, we can calculate the profiles of $D_m(r_i;\alpha)$ and $N_0(r_i;\alpha)$ from $Z_{e1}(r_i;\alpha)$. Using these $D_m(r_i;\alpha)$ and $N_0(r_i;\alpha)$, $Z_{e2}(r_i;\alpha)$ and $k_2(r_i;\alpha)$ can be obtained for the Ka-band from which we can calculate the profile of the attenuated $Z_{m2}(r_i;\alpha)$. The final step in the procedure is to adjust α to minimize the difference between the estimated $Z_{m2}(r_i;\alpha)$ and the measured $Z_{m2}(r_i)$ near the bottom of the profile. More specifically, minimize the following squared sum:

$$\sum_{i=n-m}^{n} \left[\mathrm{dB}Z_{m2}(r_i;\alpha) - \mathrm{dB}Z_{m2}(r_i)\right]^2 \tag{51}$$

where m is the number of bins from the bottom of the profile over which the difference is minimized. To reduce the error caused by the fluctuation of measured data, it is better to use a large m, but, for the estimation of the attenuation at the bottom, it is better to use a small m. In the examples shown in this article, $m = 5$ is used to estimate the attenuations. Once the best α is determined, use $D_m(r_n;\alpha)$ and $N_0(r_n;\alpha)$ as the initial values at the bottom in the backward processing. We call this method for giving the initial conditions the dual-frequency HB initialization (DHBI) method. A flow diagram of this method is depicted in Fig. 10.

V. Examples

In this section, retrieved profiles of D_m, N_w, and R from the DPR data using the proposed algorithm are shown. The PSD is assumed to follow the gamma distribution. Functions $f_1(\theta_2)$, $f_2(\theta_2)$, $g_1(\theta_2)$, and $g_2(\theta_2)$ are calculated for a collection of spherical particles with shape factors $\mu = 0, 1, 2, 3, 4$ and water temperature, T, of 0, 10, 20, and 30 °C. To avoid errors associated with measured $\mathrm{dB}Z_m$ near the noise level, only the profiles that contain $\mathrm{dB}Z_m(\mathrm{Ka}) \geq 20$ dBZ over more than ten consecutive range bins ($\equiv$1.25 km) are processed [11].

Fig. 11(a) shows an example of the vertical profiles of D_m retrieved with the proposed backward algorithm with $\mu = 3$ at

1. Calculate β for the assumed PSD by linear regression:

$$g_1(\theta_2) = a + \beta f_1(\theta_2)$$

Since $\mathrm{dB}k_1 = \theta_1 + g_1(\theta_2)$ and $\mathrm{dB}Z_{e1} = \theta_1 + f_1(\theta_2)$, if $k_1 = \alpha Z_{e1}^{\beta}$, then θ_1 and θ_2 are related as

$$\theta_1 = (\mathrm{dB}\alpha - g_1(\theta_2) + \beta f_1(\theta_2))/(1-\beta)$$

2. Define the range of processing: r_i, $i = 1, \ldots, n$.

3. Assume the value of α in $k_1 = \alpha Z_{e1}^{\beta}$.

4. Find the HB solution $Z_{e1}(r_i)$ for the Ku band.

5. Calculate $\theta_1(r_i)$ and $\theta_2(r_i)$ from $Z_{e1}(r_i)$ by using the θ_1-θ_2 ($\equiv N_0$-D_m) relation in step 1.

6. Calculate $k_2(r_i)$ and $Z_{e2}(r_i)$ from $\theta_1(r_i)$ and $\theta_2(r_i)$.

7. Calculate $Z_{mc2}(r_i)$ and compare it with $Z_{m2}(r_i)$.

8. Is $\sum_{i=n-m}^{n} |Z_{mc2}(r_i) - Z_{m2}(r_i)|^2$ small enough?

9. If 'Yes', stop and use $\theta_1(r_n)$ and $\theta_2(r_n)$ as the initial values.
If 'No', return to 3.

Fig. 10. Flow diagram of the dual-frequency DHBI method. Note that $\theta_1 = 10\log_{10} N_0$ and $\theta_2 = 10\log_{10} D_m$.

$T = 10$ °C in a stratiform area. The D_m profile from the operational V06X product is also shown by a dotted line. Three profiles are shown: one with $\mathrm{dB}Z_m$ smoothed by a nine-point Hanning filter before applying the retrieval algorithm and the other two without any smoothing to the measured Z_m data. The latter two profiles are the left-hand side solution and the right-hand side solution. It can be seen that the fluctuation of the retrieved D_m is significant without smoothing. Similar but more pronounced fluctuations appear in the N_w and R profiles [see Fig. 11(b)]. To minimize the fluctuations, the examples shown in the rest of this article are processed with the smoothed data. The example in Fig. 11 is a relatively rare case in which the left- and right-hand solutions differ in multiple bins. However, the overall profiles from these solutions are approximately the same. In this example, the liquid phase of precipitation is assumed at all heights. Therefore, D_m shown in the figure from the current algorithm in and above the bright band may not represent the true diameter. The large increase in D_m at about 5 km above sea level corresponds to the bright band. Nevertheless, it is not very much different from the true unmelted diameter in such a region because the DFR as a function of unmelted diameter is only weakly dependent on the density of ice and water particles. The major error comes from the attenuation correction in such regions that affect the estimate of DFR. Since D_m from the V06X product gives an equivalent melted diameter, it appears to be smaller than the D_m estimates from the current algorithm in solid and mixed precipitation regions.

Note that, when the left-hand side solutions of θ_2 are chosen, the corresponding estimates of R become unrealistically large in many cases. Accepting a small value of θ_2 tends to give large estimates of R. This is the reason for defining the lower

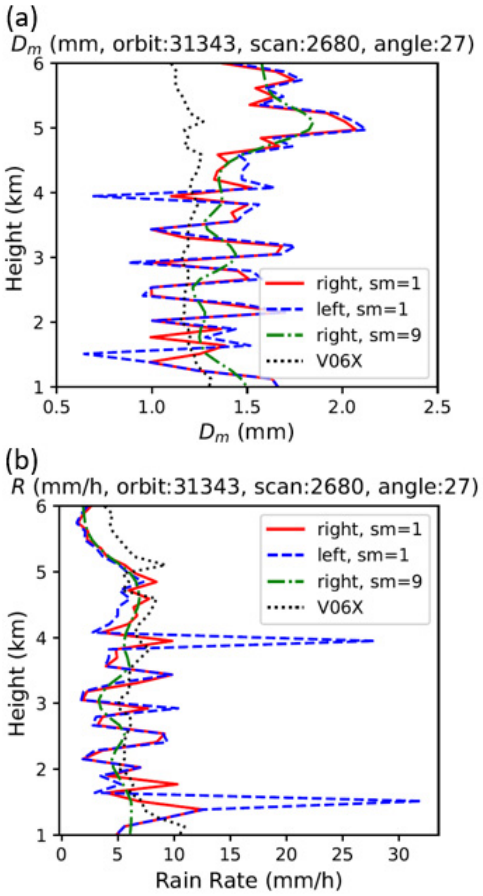

Fig. 11. Example of retrieved (a) D_m and (b) R profiles with the proposed algorithm. Note that D_m from the operational V06X shows the melted equivalent diameter, while D_m from the current algorithm shows the unmelted diameter. Key "right (left)" indicates the right-hand (left-hand) side solutions. The number of points for smoothing is denoted by "sm" in the key. The 0 °C isotherm height is 5.8 km.

limit of $\theta_{2,l} = -2$ ($\equiv D_m = 0.63$ mm). When ΔB is between L_d and L_s, there are two possible solutions. Because the solution on the left-hand side is unstable as proved previously, and it often gives discontinuous profiles as shown later, the examples shown in this article are the data estimated by choosing the right-hand side solutions all the time unless otherwise mentioned.

Fig. 12(a) shows the estimated D_m at 3 km above the sea level from DPR measurements over hurricane Dorian with the initial conditions selected by the DHBI method proposed in this article. Fig. 12(b) shows the same estimates but with the initial conditions given by the SRT. D_m estimates from the operational V06X product are shown in Fig. 12(c) for comparison. Fig. 13 shows the estimated R at 3 km above the sea level from the same datasets. The R distributions estimated from the current algorithm with the DHBI method and from the operational V06 product show quite similar distributions of R although, for the former, estimates are somewhat smaller than the latter.

The comparison between the estimates from the current algorithm and those from the operational product can be seen in Fig. 14. R and D_m shown in these scatter plots are right-hand side solutions obtained with the DHBI method in

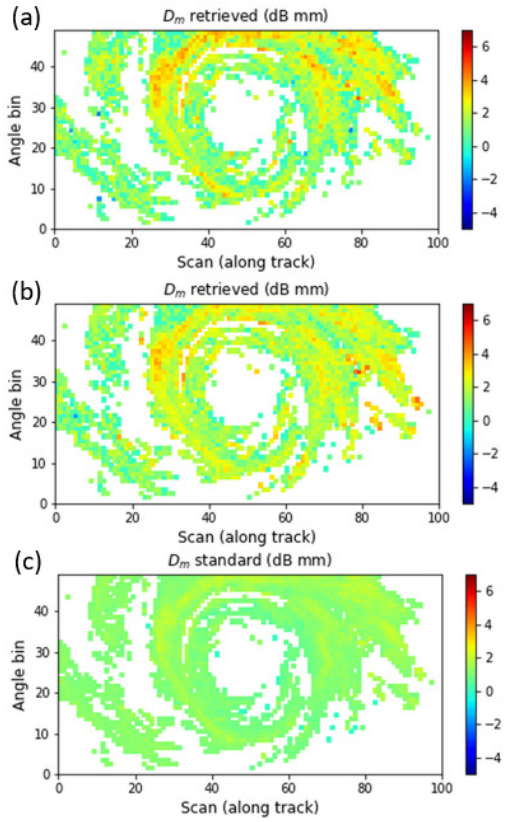

Fig. 12. Horizontal distribution of estimated D_m at $H = 3$ km from DPR measurement over hurricane Dorian (Orbit 31343, scans 2650–2749). (a) Initial conditions are determined by the DHBI method. (b) Initial conditions are determined by the SRT-PIA. (c) D_m from the operational V06X product.

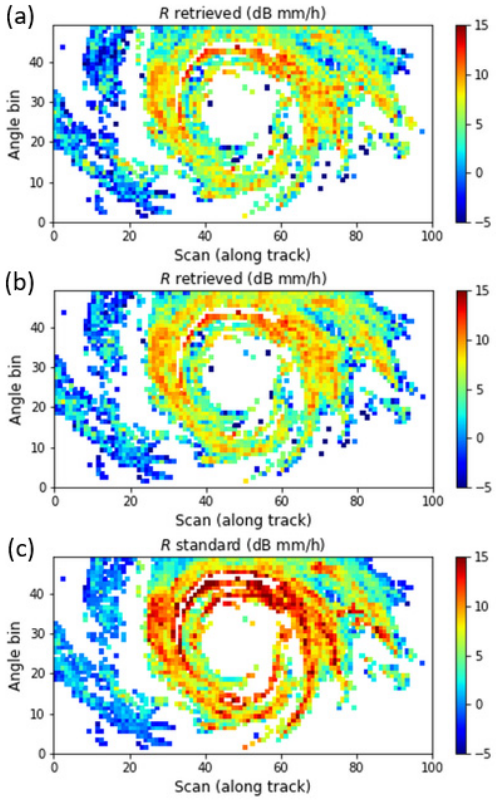

Fig. 13. Same as Fig. 12 but for the estimated rainfall rate R in dB mm/h. (a) Initial conditions are determined by the DHBI method. (b) Initial conditions are determined by the SRT-PIA. (c) D_m from the operational V06X product.

backward processing. The PIAs to the surface from the test data are on average somewhat smaller than the PIA estimates from the SRT in this example.

Since the solutions from the proposed algorithm depend on the assumed PSD, their dependence is tested with different μ values of the gamma PSD. Fig. 15 shows how the averaged vertical profiles of the retrieved parameters change with the assumed μ value for pixels with a bright band. The liquid phase is assumed at all heights. The retrieved profiles of $\mathrm{dB}D_m$, $\mathrm{dB}N_w$, R, $\mathrm{dB}Z_{e\lambda}$, and $\mathrm{dB}Z_{m\lambda}$ ($\lambda = 1, 2$) that are within 100 scans (4900 beams) in the vicinity of Hurricane Dorian and are classified as having a detectable bright band, are averaged. The figure shows cases with $\mu = 0, 1, 2, 3$, and 4, together with the output from the V06X operational product. It can be seen that the R profiles with different values of μ do not change much, in particular, when the DHBI method is used to select the initial conditions.

Similar differences are found in convective cases as well, but, in the convective cases, the differences between the estimates from the current algorithm and those from the operational product are larger. In the Dorian case, R estimates with the DHBI method is smaller than the standard product substantially. Fig. 15(c) shows average profiles of the PSD parameters from a widespread storm over land. In this case, the current algorithm with the DHBI method still tends to give smaller estimates of R than the standard method. Although the true cause of this difference in R estimates is not clear, one of the major causes can be the nonuniform beam filling (NUBF) corrections that are applied in the operational algorithm but not in the current algorithm. Nevertheless, the difference in the South American case is not as large as in the Dorian case. This kind of difference between over ocean and over land may be universal and might arise either from different PSD characteristics over ocean and land or from a possible bias in the PIA estimates by the SRT over the wet surface under rain [12], [13]. Note, however, that the magnitude of differences between the current estimates and the standard product varies even among several over-ocean storm cases that have been tested. It may be worth taking the statistics of such differences to investigate their possible relationship to the type of storm system and characteristic PSD.

These examples show to what extent the assumed μ value affects the estimates. Interestingly, the dependence on the assumed temperature of liquid precipitation is so small that the differences are not noticeable in averaged profiles like the ones shown in Fig. 15 when the temperature is changed from 0 °C to 30 °C (results not shown).

Note that D_m from the operational product shown in the figure is the melted mean diameter, whereas D_m from the current algorithm gives the actual diameter in the case of ice or mixed-phase particles. A consequence of this choice is the large D_m from the current algorithm in and near the bright band. The scattering cross sections of liquid particles are assumed even in the bright band in the data shown. The D_m profiles show that mixed-phase snow aggregates in bright band act as large liquid particles in the radar echoes. Since the profiles shown

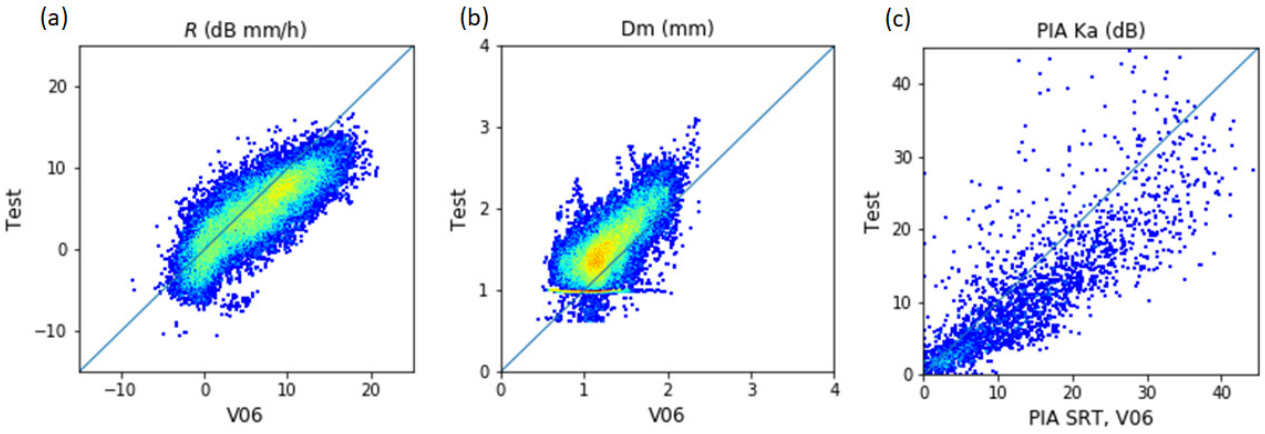

Fig. 14. Scatter plots of (a) R and (b) D_m and (c) Ka-band PIA to surface between the estimates from the proposed method with the backward processing (Test) and the corresponding parameters from the operational product (V06). Data include all storm types from the Dorian data. R and D_m data include data between 2 and 4 km above the sea surface.

are obtained by backward processing, a discrepancy in the assumption of the precipitation phase in the bright band does not affect the estimates below the bright band.

Another interesting issue is the difference between the current solutions and the operational product when the initial conditions are set by the PIA from the SRT. The reason for the discrepancy is not clear but may come from a different use of attenuation estimates. In fact, the current method uses the PIA estimates from the SRT in all cases to define the initial conditions whenever the reliability flag of SRT shows that the SRT's PIAs are reliable or marginally reliable. By contrast, the operational algorithm uses a weighted combination of the SRT/PIA and the HB estimates of attenuation. The application of an NUBF correction in the operational algorithm may also contribute to differences, particularly in convective cases.

VI. Discussion

Several issues in the dual-frequency PSD retrieval algorithm are discussed in this section.

A. Noise

The major noise component in the DPR received power is fading noise. Since the log-averaged power is recorded, the signal fluctuates around the mean with a Gaussian distribution in the dB scale. Since $\mathrm{dB}D_m$ and $\mathrm{dB}Z_e$ are approximately linearly correlated, estimates of D_m also fluctuate similarly in the dB scale if no smoothing is applied to the measured data. If R is calculated directly from the estimated D_m and N_0 and expressed in the linear scale, its positive deviations are generally larger than the negative deviations due to the nonlinear transformation of $\mathrm{dB}R$ to R, and the average of R is slightly larger than R calculated from the average of $\mathrm{dB}R$ (Jensen's inequality). The final estimates of R, D_m, or N_w depend somewhat on at which stage we take the average to reduce the fluctuation errors. In the examples shown in this article, the measured $\mathrm{dB}Z_m$'s are smoothed with a nine-point Hanning filter (i.e., over ± 0.5 km). No other smoothing is applied. The choice of the Hanning filter is arbitrary. It is adopted because the smearing of curved profiles, such as those near the peak of the bright band, is smaller than the flat moving average. Other filters, such as the Savitzky–Golay filter that preserves the signal tendency relatively well, can be used as well.

The dual-frequency algorithm assumes that echoes at two frequencies are available at all range bins. This condition is not met all the time. In fact, quite often, because of the sensitivity difference and a significant attenuation at the higher frequency channel, meaningful echoes are available only at a single frequency at many range bins. As mentioned before, only the profiles that give more than ten continuous range bins with $\mathrm{dB}Z_m$(Ka) larger than 20 dBZ are processed in the examples shown in this article.

B. Dual-Solution

We show in Section II that small errors in initial conditions either shrink or increase only moderately in the backward processing if $D_m > D_{mc}$ and $\mathrm{dB}Z_e(\mathrm{Ku}) > 20$ dBZ. Since the majority of rain cases measurable with the DPR belong to this domain, it is natural to use backward processing. Unless otherwise stated, the examples shown in this article are processed with the algorithm that chooses the solution in domain II ($\theta_2 > \theta_{2,d}$, right-hand side solution) rather than in domain I ($\theta_2 < \theta_{2,d}$, left-hand side solution) whenever there are two possible solutions. Stability is another reason for choosing the solution in domain II. If we choose the left-hand side solutions in backward processing, an interesting phenomenon happens. Fig. 16 shows a retrieved profile of $\mathrm{dB}D_m$ and $\mathrm{dB}N_0$ from a pair of synthetic $\mathrm{dB}Z_{m,\lambda}$ profiles. These synthetic data are created by the condition that $\mathrm{dB}Z_e(\mathrm{Ku}) = 30$ dBZ and $\mathrm{dB}D_m$ changes linearly with range. The broken lines show the true profiles, and the solid lines show the retrieved profiles. The true $\mathrm{dB}D_m$ varies from domain II to I as the range decreases. The backward retrieved solution oscillates between just above $\theta_{2,l}$ and just above $\theta_{2,s}$. This phenomenon happens because, when the solution is in domain I, the solution at the next step tends to move toward $\theta_{2,l}$ by increasing ΔB. However, a small increase in ΔB often results in the case in which the solution exists only in domain III ($\theta_2 > \theta_{2,s}$) because ΔB becomes larger than L_s. Once the solution is in domain III, the algorithm tries to find the next solution with

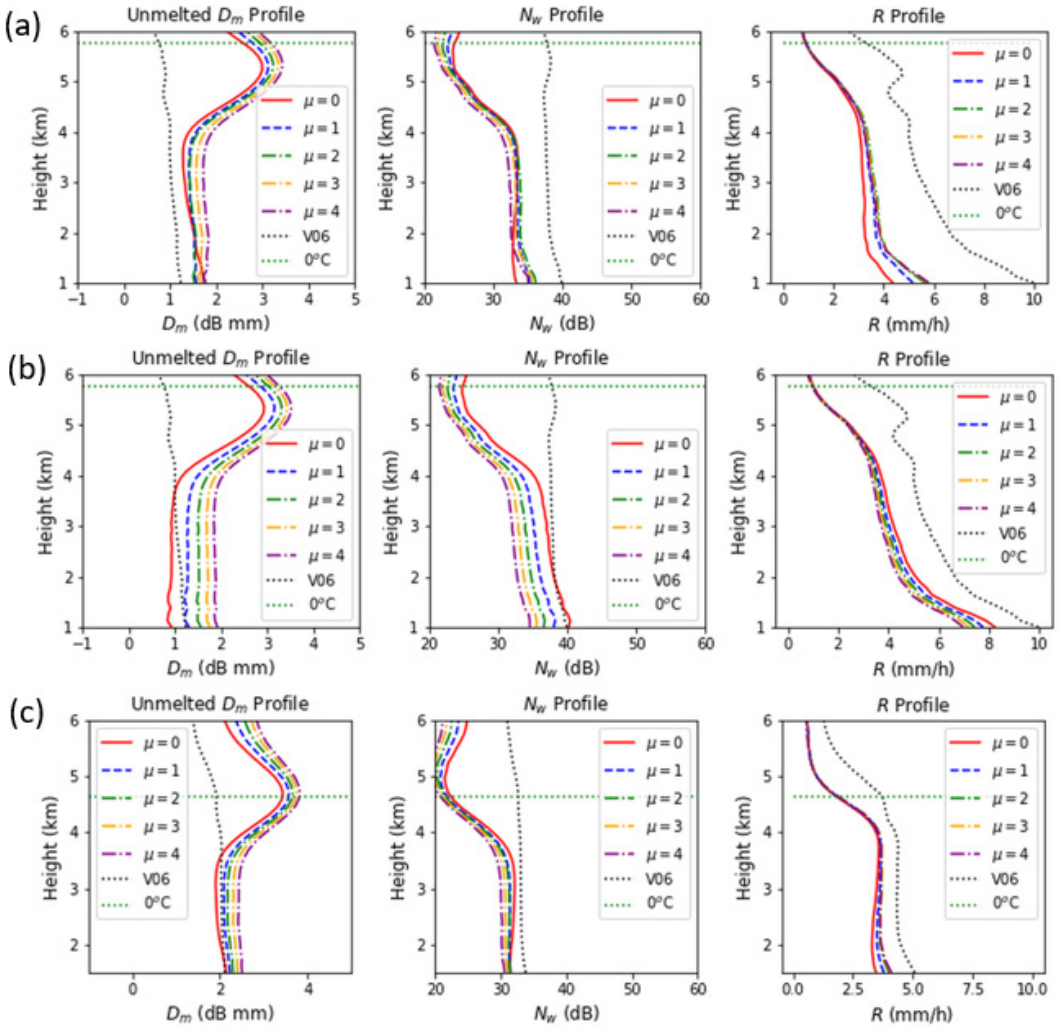

Fig. 15. Dependence of the averaged vertical profiles of D_m, N_w, and R of rain pixels identified with bright bands on the shape factor μ. The dotted lines show the profiles from the operational products V06X. D_m is the unmelted diameter expressed in dB mm except for the operational V06X in which D_m is the melted diameter. (a) Data from DPR measurement over hurricane Dorian (Orbit 31343, scan 2650–2749, September 4, 2019, east of Florida). The initial conditions are determined by the proposed DHBI method. (b) Same as (a), but the initial conditions are determined by the PIA estimates with the surface reference method. (c) Data from a widespread storm over land (Orbit 39356, scan 6500–6599, January 31, 2021, center at Lat = −24.7, Lon = −54.3, South America). The initial conditions are determined by the DHBI method. The 0 °C isotherm height from V06X products is shown by a horizontal green dotted line.

a smaller ΔB and decreases D_m. As soon as ΔB becomes smaller than $L_s = L_B(\theta_{2,s})$, two solutions are possible, and the solution in domain I is chosen by rule. This cycle is repeated. As the figure shows, the reproduced dBZ_m profiles agree nearly perfectly with the given measured profiles because the true attenuations are given by the initial conditions. The retrieved dBZ_e profiles are nearly identical to the original profiles.

This simple example indicates that the reproducibility of Z_m profiles does not guarantee the correctness of the retrieved parameters. Furthermore, the uncertainty in each estimate of D_m must be rather large when we think about the fluctuation of measured signals and the small gradient of $L_B(\theta_2)$ in domain I and II.

Fig. 17(a) and (b) shows the contoured frequency by altitude diagrams (CFADs) of D_m obtained by the right-hand side solutions and the left-hand side solutions by the backward processing, while Fig. 17(c) shows that by the forward processing. The assumed phase state of the particles in the retrieval algorithm is changed from liquid to solid abruptly at $H = 5.5$ km, which is slightly above the center of the bright band.

In this kind of light precipitation case in a stratiform system in which attenuation is minimal, the DFRm method and the forward processing give nearly identical estimates of D_m in the solid precipitation region, as demonstrated in Fig. 9. The backward processing deviates from the forward solutions or the DFRm method in many cases. The D_m estimates by the backward processing often end up at the lower bound ($\theta_{2,l}$) of the searching domain in the solid precipitation region, as can be seen in Fig. 17(a). This discrepancy results most likely from the fact that the attenuation estimated at the bright band top by the backward processing is biased due to an inappropriate attenuation model through the bright band. Although the estimates are biased, however, the variation of D_m with altitude by the backward processing is similar to the forward solutions. The discrepancy of D_m in the solid

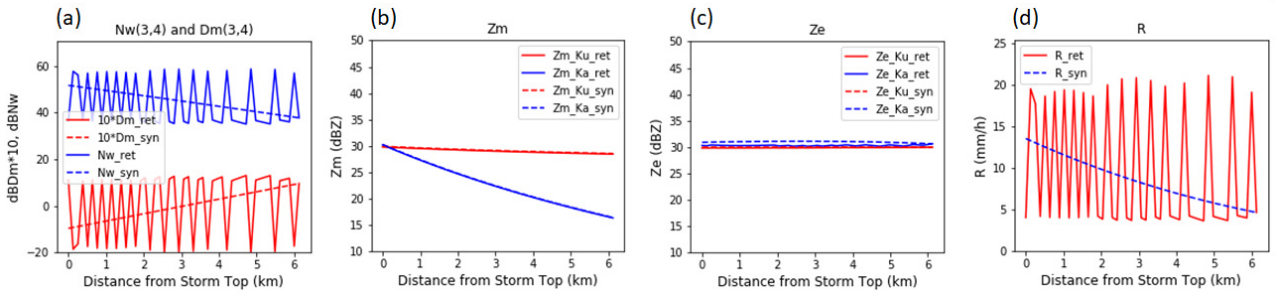

Fig. 16. Behavior of left-hand side solutions in the backward processing when the true D_m changes linearly in the dB scale with range from domain I to II. The true dBZ_e(Ku) is assumed constant at 30 dBZ. Input data of dBZ_m(Ku) and dBZ_m(Ka) are synthesized from these conditions with a $\mu = 3$ gamma PSD model. Solutions for (a) N_w and D_m, (b) Z_m, (c) Z_e, and (d) R.

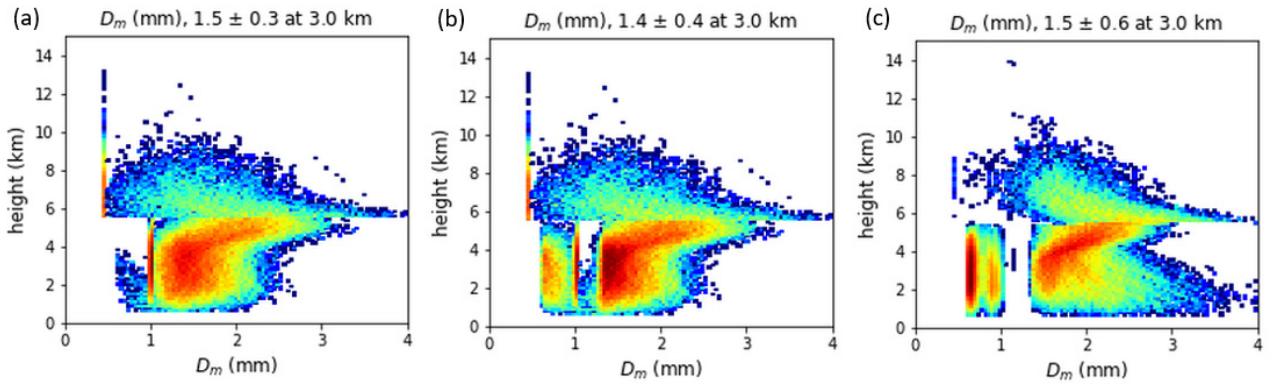

Fig. 17. CFADs of estimated D_m from (a) right-hand side solutions, (b) left-hand side solutions by the backward processing, and (c) left-hand side solutions by the forward processing. The assumed phase state of the particles in the retrieval algorithm is changed from liquid to solid abruptly at $H = 5.5$ km. The 0 °C isotherm height is 5.8 km.

precipitation region between the forward processing and the backward processing cannot be resolved no matter the height at which the assumed phase is changed from liquid to solid in the backward processing. It seems necessary to introduce a layer in the bright band in which the specific attenuations at Ku- and Ka-bands take a rather different ratio than that given by a simple liquid particle model. Note that there are many solutions that end up at the maximum diameter of 4 mm at low altitude in the forward processing because of the divergent tendency of the forward solutions in the liquid precipitation region. It is also worth noting that the left-hand side solutions in domain I in the forward processing do not diverge to the minimum allowable value of $\theta_{2,l} = -2$ ($D_m = 0.63$ mm), unlike the left-hand side solutions in the backward processing.

The estimates of D_m in these figures are obtained by assuming the density of snow as $\rho = 0.2$ g/cm^3. As mentioned before, these estimates are relatively insensitive to the assumed value of ρ. However, the corresponding N_w estimates depend on the value of ρ because Z_e for a given D_m depends on ρ. Therefore, even though the discontinuity of the estimated unmelted D_m at $H = 5.5$ km is not very large, the corresponding N_w estimates show a very clear discontinuity at this height (not shown). To estimate continuous and realistic N_w, we need further information or assumptions in the phase transition layer and above.

As mentioned in Section III, the proposed algorithm does not solve the dual-solution problem entirely. Nevertheless, when the attenuation within the bin is large enough, $L_B(\theta_2)$ becomes a monotonically increasing function of θ_2, and the dual-solution problem disappears. In fact, with the Dorian data shown in this article, there are about 50 000 pairs of adjacent bins in the rain region that satisfies the conditions for testing the algorithm. Of these 50 000 adjacent pairs, if we use $\Delta r = 0.125$ km, function $L_B(\theta_2)$ becomes a monotonically increasing function in about 9% of the pairs. In the remaining 91%, $L_B(\theta_2)$ is not monotonic, but the actual solutions are in the single solution domain III ($\theta_2 > \theta_{2,s}$) more than 80% of the cases, and the dual solutions ($\theta_2 < \theta_{2,s}$) occur in only about 10% of the total cases. Increasing the range bin size will increase the attenuation between adjacent bins and lower the condition for $L_B(\theta_2)$ to be a monotonic function. If we use $\Delta r = 0.5$ km, for example, the number of cases with a monotonically increasing $L_B(\theta_2)$ increases to 30%, and the dual-solution cases decrease to about 7%. If we use every pair of dBZ_m separated by eight range bins so that $\Delta r = 1$ km, the number of cases with a monotonically increasing $L_B(\theta_2)$ increases to 47%. In the remaining 53% of the total cases, 41% of the total cases are in the single solution domain III, no solution case ($\Delta B < L_d$) occurs in 7% of solutions, and only 4% of total cases are subject to the dual-solution problem. The latter number decreases to 1% if the threshold of processing Ka data is increased to 25 from 20 dBZ. In the South American case, these numbers are 58%, 38%, 3%, and 1% so that the double-solution cases become very rare.

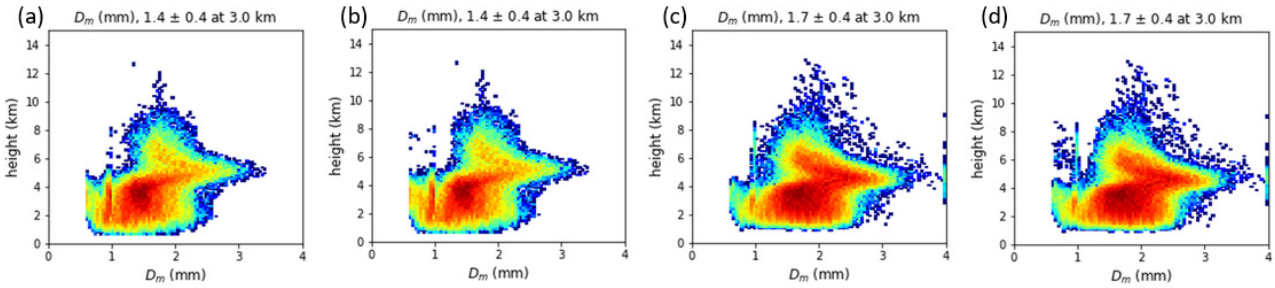

Fig. 18. CFADs of estimated D_m for the hurricane Dorian case [(a) and (b)] and South American storm case [(c) and (d)] from right-hand side solutions [(a) and (c)] and left-hand side solutions [(b) and (d)] by the backward processing with $\Delta r = 1$ km. The liquid phase of precipitation is assumed in the entire range. The 0 °C isotherm height is 5.8 km in the Dorian area and 4.6 km in the South American storm.

Fig. 18 shows CFADs of D_m from the Dorian and South American cases when $\Delta r = 1$ km is used. Because of the increase in the single solution cases, the left- and right-hand side solution cases show nearly the same distributions in both cases. Judging from their distributions in rain regions below 4 km, we can observe that D_m is in domain II rather than domain I in the majority of cases when $\Delta B < L_s$. In addition to the stability issue, this observation is another reason for selecting the right-hand side solutions as the solutions of this algorithm in the examples in this article. However, increasing the step size may violate the assumption of rain uniformity and may result in an adverse effect. In fact, $\Delta r = 1$ km is too large to estimate the PSD parameters in and around the bright band where the specific attenuation at the Ka-band can change significantly over a short distance.

C. Uncertainties in PSD and Scattering Model

If valid Z_m data are available at two frequencies at n range bins, we have at most $2n$ independent pieces of information. This fact implies that we can estimate only up to $2n$ parameters. In the current case, we choose D_m and N_0 at n range gates. All other parameters that affect the retrieval must be assumed in some way. For example, they must be defined as functions of D_m and N_0 or given by environmental data independently provided. In the current case, we need to assume the functions $f_1(\theta_2)$, $f_2(\theta_2)$, $g_1(\theta_2)$, and $g_2(\theta_2)$. These functions depend on the PSD and scattering properties of individual particles. The latter depends on the phase, melting fraction, density, shape, and temperature of precipitating particles. In particular, since the specific attenuation depends on the phase state substantially, phase identification becomes crucial for accurate estimation.

Liao *et al.* [2] show that the snow density does not strongly affect the dependence of DFR on D_m when the DFR is taken between X- and Ka-bands although the DFR changes somewhat with the shape factor μ of the assumed gamma PSD. These characteristics of DFR dependence on the snow density and the shape factor are the same for the DFR taken between Ku- and Ka-bands. Therefore, unmelted D_m values estimated by assuming $\rho = 0.2$ g/cm^3 do not change significantly even if we assume a different ρ value. However, the melted D_m and N_0 depend on the assumed value of ρ.

As to the estimated D_m for rain, it depends slightly on the assumed temperature of drops because the minimum values of both DFR and DFk depend on the temperature, as depicted in Fig. 1. However, since the differences due to the temperature difference are small except near the minimum point of those functions, the estimated D_m does not change much even if we change the assumed temperature from 0° to 30°. (D_m at the minimum of DFR changes from 1.00 to 1.02 mm when the temperature changes from 0 °C to 30 °C if $\mu = 3$.) The estimated D_m depends more on the assumed value of the shape factor μ. (D_m at the minimum of DFR changes from 0.78 to 1.07 mm when μ changes from 0 to 4 when the temperature is 10 °C.) This dependence on μ is more problematic because the actual PSD changes substantially, and the dependences of k and Z_e on D_m and N_0 deviate from those derived from any PSD model functions. As a result, even if the true rain is vertically uniform and the attenuation correction is properly applied to determine the initial conditions, the estimated PSD profiles may result in some bias in their absolute values and their vertical gradient.

In a region of dry snow in which attenuation can be effectively ignored, however, the issue is not very severe. We can estimate the unmelted diameter D_m from DFRm as mentioned before. The property mentioned in the previous paragraph may be used to identify the existence of hail and graupel by looking at retrieved D_m and Z_e values as long as the particles are dry. However, if some wet hail exists, the problem becomes formidable. Large hailstones may add multiple scattering echoes that make the problem even more difficult. How to deal with such cases is an interesting issue but outside the scope of this article.

We have shown that the right-hand side solutions in the backward processing are stable or only moderately divergent as long as D_m is larger than the critical diameter of about 1 mm and estimate D_m in rain region reasonably well. However, the estimates within the bright band may not be accurate because of uncertainties in the scattering characteristics in the transition layer from solid to liquid phase. To estimate D_m within and above the bright band in the backward processing, appropriate PSD and scattering models are required.

Both NUBF and multiple scattering change the apparent dependence of k and Z_e on D_m and N_0. In particular, the effective k is no longer a local function of D_m and N_0 but depends on the 3-D distribution of precipitation. As a result, attenuation correction becomes a formidable task, and reliable correction is virtually impossible when these effects are significant. Since k cannot be expressed in terms of D_m and N_0 locally, the

current formulation would require some modifications in such cases.

D. Initial Values

As mentioned in the algorithm section, the solutions of the proposed method depend critically on the initial values. A self-consistent DHBI method to estimate the attenuations to the bottom bin is proposed and tested. This initialization method, however, depends on the assumed vertical profile of phase state although its effect is not significant because the attenuation from solid precipitation range to the total path attenuation is generally rather small. Nevertheless, there is room for improvement. There may be a better way to find initial values of D_m and N_0 at the bottom in the backward processing. If estimation with a fixed PSD model and other simplifying assumptions, such as no NUBF or multiple scattering effects, does not give reliable estimates, improvement of the initialization method alone will not further improve the estimates. Although better ways to specify the initial conditions have not been pursued, further work along these lines is warranted.

E. Other Possibilities

In this article, we discussed a method for estimating θ_1 and θ_2 as functions of range by solving equation (2) with (3) and (4) in terms of differential equations or discretized difference equations. In these methods, solutions are derived from one range to the next successively. There is a possibility, however, that $2n$ unknowns $\theta_{1,i}$ and $\theta_{2,i}$ can be determined by minimizing the difference between measured reflectivities and calculated ones without assuming any continuity

$$\sum_{i=1}^{N} \sum_{\lambda=1,2} [\mathrm{dB}Z_{m\lambda}(r_i) - \mathrm{dB}Z_{mc\lambda}(\theta_1(r_i), \theta_2(r_i))]^2 \qquad (52)$$

where $\mathrm{dB}Z_{mc,\lambda}$ denotes the calculated measured radar reflectivity factor. This method does not work in practice because of the following reasons. First, there are many local minimum points in the $2n$-dimensional space of $\theta_{1,i}$ and $\theta_{2,i}$. The double-value problem associated with DFR also contributes to this problem. It is not easy to find the global minimum point by any numerical methods even if the model assumptions are perfect. Even when there is no noise, the global minimum point is not a sharply defined minimum in some directions in the $2n$-dimensional space. The existence of noise in actual data further complicates the distribution of minimum points and may often result in profiles of θ_1 and θ_2 that are rather different from the true profiles. Additional continuity constraints that allow only small changes of the parameters between adjacent bins reduce the acceptable minimum points for the solution but do not eliminate the multiplicity of solutions. These methods also share the same issues mentioned in this section.

VII. Conclusion

General properties of retrieving two PSD parameters from matched beam dual-frequency radar data are reviewed, and a specific PSD retrieval algorithm for the DPR is proposed. An equation is derived, which expresses the relationship of the PSD parameters between the adjacent range bins, including the attenuation effect within the bin. This algorithm estimates the mean diameter of particles by solving the equation in one step from the measured radar reflectivity factors at two frequencies and the PSD parameters in the adjacent bin. In the past attempts for estimating the PSD parameters, the attenuation correction and the estimation of D_m are carried out in different steps so that recursive processing is needed in order to include the attenuation effect within the bin itself.

The stability of the solutions to the equation is examined. It is shown that the stability depends on the location of the true D_m in the case of liquid precipitation. A small gradient of D_m with respect to the range may alter the stable domains of solutions substantially from the constant D_m case. Nevertheless, if D_m is larger than the critical diameter D_{mc}, which is about 1 mm, the backward processing provides either a stable solution in which the initial errors decreases or a solution whose error increases only marginally with the processing distance. In contrast to backward processing, the forward processing gives stable or moderately diverging solutions for $D_m < D_{mc}$ and diverging solutions for $D_m > D_{mc}$. As a result, errors in the forward processing tend to increase substantially with the range in the majority of rain profiles measurable with the DPR.

It is also shown that, when the attenuation within the bin is sufficiently large, the backward function $L_B(\theta_2)$ becomes a monotonically increasing function of θ_2 so that the double-value problem disappears. However, if we use the range step size of 0.125 km, the double-value problem remains in many cases in the DPR data. Therefore, the double-value problem cannot totally be avoided. If the echo profiles are relatively uniform, by increasing the step size, the double-value problem is mitigated in most cases for the signal levels detectable by the DPR.

As a method to provide a set of initial conditions in the backward processing, an attenuation estimation method based on the HB attenuation correction method is proposed and tested. This approach gives reasonable initial conditions, and the average of estimated R agrees reasonably well with that estimated with the PIA from the SRT. Since the selection of the initial values has a decisive impact on the solutions, further study may be needed to find a better initialization method.

It is also shown that, if the attenuations to the bottom bin are well estimated, the retrieved profiles of R are nearly independent of the shape factor of the gamma PSD model even though the estimated D_m and N_0 profiles change with the μ value. If the NUBF correction is excluded, the current algorithm produces reasonable R estimates that mostly agree with the corresponding estimates from the operational products on average even though there are some differences in the estimates of D_m and N_w. We find some bias in the case of Hurricane Dorian. Since the conditions adopted in the test runs shown in this article are different from those in the operational processing due to the rather complicated conditions used in the latter algorithm, some differences are not surprising. Nevertheless, the current algorithm may provide a tool to investigate the validity of various assumptions used in the

operational algorithm. It may also be used to study the PSD in other more complicated cases, such as convective storms with hail and graupel.

APPENDIX
USE OF PIAS TO THE SURFACE AS THE INITIAL CONDITIONS

In the backward equations, we need to give appropriate initial conditions at the farthest range. If the PIA is available at two frequencies, we can give such initial conditions. We assume that $Z_{e\lambda}$ ($\lambda = 1$ for the Ku-band and $\lambda = 2$ for the Ka-band) is constant from the farthest bin (r_n) to the actual surface (r_s). Let the distance from the center of the clutter-free bottom bin to the actual surface be Δr_s

$$\Delta r_s \stackrel{\text{def}}{=} r_s - r_n. \tag{A.53}$$

Then,

$$\begin{aligned} \mathrm{dB}Z_{e\lambda,n} &= \mathrm{dB}Z_{m\lambda,n} + A_{\lambda,n} \\ &= \mathrm{dB}Z_{m\lambda,n} + \mathrm{PIA}_{\lambda,s} - [\mathrm{PIA}_{\lambda,s} - A_{\lambda,n}] \end{aligned} \tag{A.54}$$

where $\mathrm{PIA}_{\lambda,s}$ is the PIA to the surface for frequency λ. Since we assume that $Z_{e\lambda}$ is constant between r_n and r_s

$$\begin{aligned} \mathrm{PIA}_{\lambda,s} - A_{\lambda,n} &= 2\Delta r_s k_{\lambda,n} \\ &= 2\Delta r_s \exp(q(\theta_{1,n} + g_\lambda(\theta_{2,n}))). \end{aligned} \tag{A.55}$$

Substitution of (A.55) into (A.54) gives

$$\mathrm{dB}Z_{e\lambda,n} = \mathrm{dB}Z_{m\lambda,n} + \mathrm{PIA}_{\lambda,s} - 2\Delta r_s k_{\lambda,n} \tag{A.56}$$

or in terms of $\theta_{1,n}$ and $\theta_{2,n}$

$$\begin{aligned} \theta_{1,n} + f_\lambda(\theta_{2,n}) = \mathrm{dB}Z_{m\lambda,n} + \mathrm{PIA}_{\lambda,s} \\ - 2\Delta r_s \exp(q(\theta_{1,n} + g_\lambda(\theta_{2,n}))). \end{aligned} \tag{A.57}$$

Therefore, replacing Δr_i by $2\Delta r_s$ and B_λ by

$$B'_\lambda = \mathrm{dB}Z_{m\lambda,n} + \mathrm{PIA}_{\lambda,s}, \quad (\lambda = 1, 2) \tag{A.58}$$

we can find the solutions at range n.

ACKNOWLEDGMENT

The authors would like to thank Drs. Scott Braun and Erich Stocker of the NASA Goddard Space Flight Center for their support of this study.

REFERENCES

[1] A. Y. Hou *et al.*, "The global precipitation measurement mission," *Bull. Amer. Meteorol. Soc.*, vol. 95, pp. 701–722, May 2014, doi: 10.1175/BAMS-D-13-00164.1.

[2] L. Liao, R. Meneghini, T. Iguchi, and A. Detwiler, "Use of dual-wavelength radar for snow parameter estimates," *J. Atmos. Ocean. Technol.*, vol. 22, no. 10, pp. 1494–1506, Oct. 2005.

[3] T. Kubota *et al.*, "Cloud assumption of precipitation retrieval algorithms for the dual-frequency precipitation radar," *J. Atmos. Ocean. Technol.*, vol. 37, pp. 2015–2031, 2020, doi: 10.1175/JTECH-D-20.0041.1.

[4] R. Meneghini *et al.*, "Use of the surface reference technique for path attenuation estimates from the TRMM precipitation radar," *J. Appl. Meteorol.*, vol. 39, no. 12, pp. 2053–2070, Dec. 2000, doi: 10.1175/1520-0450(2001)040<2053:UOTSRT>2.0.CO;2.

[5] S. Seto *et al.*, "The precipitation rate retrieval algorithms for the GPM dual-frequency precipitation radar," *J. Meteorol. Soc. Jpn. Ser.*, vol. 99, no. 2, pp. 205–237, 2021, doi: 10.2151/jmsj.2021-011.

[6] J. Testud, S. Oury, R. A. Black, P. Amayenc, and X. Dou, "The concept of 'normalized' distribution to describe raindrop spectra: A tool for cloud physics and cloud remote sensing," *J. Appl. Meteorol. Climatol.*, vol. 25, no. 10, pp. 1118–1140, 2001, doi: 10.1175/1520-0450(2001)040<1118:TCONDT>2.0.CO;2.

[7] G. Lee, I. Zawadzki, W. Szyrmer, D. Sempere-Torres, and R. Uijlenhoet, "A general approach to double-moment normalization of drop size distributions," *J. Appl. Meteor.*, vol. 43, pp. 264–281, 2004, doi: 10.1175/1520-0450(2004)043<0264:AGATDN>2.0.CO;2.

[8] M. W. Hirsch, S. Smale, and R. L. Deveney, *Differential Equations, Dynamical Systems, and an Introduction to Chaos*. Waltham, MA, USA: Academic, 2013.

[9] W. Hitschfeld and J. Bordan, "Errors inherent in the radar measurement of rainfall at attenuating wavelengths," *J. Meteorol.*, vol. 11, no. 1, pp. 58–67, Feb. 1954.

[10] T. Iguchi and R. Meneghini, "Intercomparison of single-frequency methods for retrieving a vertical rain profile from airborne or spaceborne radar data," *J. Atmos. Ocean. Technol.*, vol. 11, pp. 1507–1516, 1994, doi: 10.1175/1520-0426(1994)011<1507:IOSFMF>2.0.CO;2.

[11] T. Masaki *et al.*, "Calibration of the dual-frequency precipitation radar (DPR) onboard the global precipitation measurement (GPM) core observatory," *IEEE Trans. Geosci. Remote Sens.*, vol. 60, 2021, Art. no. 5100116, doi: 10.1109/TGRS.2020.3039978.

[12] S. Seto and T. Iguchi, "Rainfall-induced changes in actual surface backscattering cross sections and effects on rain-rate estimates by spaceborne precipitation radar," *J. Atmos. Ocean. Technol.*, vol. 24, no. 10, pp. 1693–1709, Oct. 2007, doi: 10.1175/JTECH2088.1.

[13] S. Seto, T. Iguchi, and R. Meneghini, "Correction of path integrated attenuation estimates considering the soil moisture effect for the GPM dual-frequency precipitation radar," *J. Atmos. Ocean. Technol.*, Mar. 2022, doi: 10.1175/JTECH-D-21-0111.1.

Toshio Iguchi (Fellow, IEEE) received the B.Sc. degree from Hokkaido University, Sapporo, Japan, in 1976, the M.Sc. degree from the University of Tokyo, Tokyo, Japan, in 1978, and the Ph.D. degree from York University, Toronto, ON, Canada, in 1983.

From 1985 to 2019, he was with the National Institute of Information and Communications Technology, Koganei, Japan. He visited the National Aeronautics and Space Administration (NASA)/Goddard Space Flight Center, Greenbelt, MD, USA, from 1991 to 1994, performing the U.S.–Japan collaborative experiment for measuring rain using airborne radar. He is a Visiting Research Scientist within the Department of Earth System Science Interdisciplinary Center, University of Maryland, College Park, MD. His work has been mainly related to remote sensing of the environment, in particular, issues related to the remote sensing of precipitation from space. He has served on the science teams for the Tropical Rainfall Measuring Mission (TRMM) and GPM since their inception and has developed operational radar algorithms for both radars.

Robert Meneghini (Senior Member, IEEE) is an Employee with the National Aeronautics and Space Administration (NASA) Goddard Space Flight Center, Greenbelt, MD, USA. With scientists from the Communications Research Laboratory of Japan, he co-led a series of airborne field campaigns from 1985 to 2000, the data from which were used to develop algorithms for the TRMM and GPM spaceborne weather radars. He has served on the science teams for TRMM and GPM since their inception and has developed operational radar algorithms for both radars. His research interests include scattering theory, rain and snow retrievals from active and passive instruments, and the use of radar for wind estimation over the ocean.